QUANTUM ENTANGLEMENT AND LIGHT PROPAGATION THROUGH BOSE-EINSTEIN CONDENSATE(BEC)

A THESIS

SUBMITTED TO THE DEPARTMENT OF PHYSICS

AND THE INSTITUTE OF ENGINEERING AND SCIENCE

OF BILKENT UNIVERSITY

IN PARTIAL FULFILLMENT OF THE REQUIREMENTS

FOR THE DEGREE OF

DOCTOR OF PHILOSOPHY

By

Mehmet Emre Taşgın
September 2009

I certify that I have read this thesis and that in my opinion it is fully adequate, in scope and in quality, as a dissertation for the degree of doctor of philosophy.

Assoc. Prof. Dr. Mehmet Özgür Oktel (Supervisor)

I certify that I have read this thesis and that in my opinion it is fully adequate, in scope and in quality, as a dissertation for the degree of doctor of philosophy.

Prof. Dr. Bilal Tanatar

I certify that I have read this thesis and that in my opinion it is fully adequate, in scope and in quality, as a dissertation for the degree of doctor of philosophy.

Assoc. Prof. Dr. Ceyhun Bulutay

I certify that I have read this thesis and that in my opinion it is fully adequate, in scope and in quality, as a dissertation for the degree of doctor of philosophy.

Assoc. Prof. Dr. Bayram Tekin

I certify that I have read this thesis and that in my opinion it is fully adequate, in scope and in quality, as a dissertation for the degree of doctor of philosophy.

Assoc. Prof. Dr. Ergün Yalçın

Approved for the Institute of Engineering and Science:

Prof. Mehmet Baray,
Director of Institute of Engineering and Science

Abstract

QUANTUM ENTANGLEMENT
AND
LIGHT PROPAGATION
THROUGH
BOSE-EINSTEIN CONDENSATE(BEC)

Mehmet Emre Taşgın
PhD in Physics
Supervisor: Assoc. Prof. Dr. Mehmet Özgür Oktel
September 2009

We investigate the optical response of coherent media, a Bose-Einstein condensate (BEC), to intense laser pump stimulations and weak probe pulse propagation.

First, we adopt the coherence in sequential superradiance (SR) as a tool for continuous-variable (CV) quantum entanglement of two counter-propagating pulses from the two end-fire modes. In the first-sequence the end-fire and side mode are CV entangled. In the second sequence of SR, this entanglement is swapped in between the two opposite end-fire modes.

Second, we investigate the photonic bands of an atomic BEC with a triangular vortex lattice. Index contrast between the vortex cores and the bulk of the condensate is achieved through the enhancement of the index via atomic coherence. Frequency dependent dielectric function is used in the calculations of

the bands. We adopt a Poynting vector method to distinguish the photonic band gaps from absorption/gain regimes.

Keywords: superradiance, quantum entanglement, continuous variable, condensate, photonic crystal, band gap, frequency dependent dielectric.

Özet

BOSE-EINSTEIN YOĞUŞMASI (BEY) ÜZERİNDE
IŞIĞIN YAYILIMI
VE KUVANTUM DOLAŞIKLIĞI

Mehmet Emre Taşgın
Fizik Doktora
Tez Yöneticisi: Doç. Dr. Mehmet Özgür Oktel
Eylul 2009

Bu çalışmamızda faz uyumlu (koherent) ortam olan Bose-Einstein Yoguşması'nın (BEY'in) yüksek şiddetteki lazer uyarımlarına ve zayıf şiddetteki test pulsuna (darbesine) verdigi optik tepkiyi incelemekteyiz.

İlk olarak, sıralı Süperışımadaki (SI) faz uyumluluğunu, iki uç-ateş modundan (kipinden) çıkıp birbirlerine zıt yönde yayılan pulsların, sürekli-değişkenli (SD) kuvantum dolaşıklılığını oluşturmakta kullanmaktayız. Işımanın ilk sırasında uç-ateş foton ve atom yan-modları birbirine dolaşmaktadır. Işımanın ikinci sırasında ise, bu atom-foton SD dolaşıklıgı zıt yönlü iki uç-ateş modlarına aktarılmaktadır.

İkinci olarak, üçgensel örgüye sahip atomik BEY'e ait vorteks (girdap) periyodik örgüsünün fotonik bant yapısını incelemekteyiz. Vorteks çekirdeği ve yoğuşma kütlesi arasındaki optik indeks farkı, indeksin atomik faz uyumluluğu kullanılarak güçlendirilmesiyle elde edilmektedir. Bant hesaplarımızda frekans-bağımlı dielektrik fonksiyon kullanılmıştır. Fotonik bant boşluklarını

soğurma/kazanç rejimlerinden ayırt edebilmek için Poynting vektör incelemesine dayanan yeni bir metod kullanmaktayız.

Anahtar sözcükler: süper ışıma, kuvantum dolaşıklığı, sürekli değişkenli, yoğuşma, fotonik örgü, bant boşluğu, frekansa bağlı dielektrik.

Acknowledgement

I would like to express my deepest gratitude and respect to my supervisors Prof. M. Özgür Oktel and Prof. Özgür E. Müstecaplıoğlu for their guidance and understanding during my Ph.D. study. I am also thankful to my undergraduate supervisor Prof. Bilal Tanatar.

I would present my specially thanks to Ceyhun Bulutay, the motivating Professor of the department, for his encouraging words during the whole twelve years. Without him academic life would be insufferably hard.

I am thankful to Prof. Salim Çıracı, the founder of the Department of Physics and Faculty of Science.

I would like to thank all of my friends, with whom I spent enjoyable time: Kurtuluş Abak, Can Ataca, Koray Aydın, Selcen Aytekin, Duygu Can, Seymur Cahangirov, Deniz Çakır, Itır Çakır, Engin Durgun, Yeter Hanim, Murat Keçeli, Ahmet Keleş, Ümit Keleş, Hakan Kıymazaslan, Aşkın Kocabaş, Rasim V. Ovalı, Barış Öztop, Erçağ Pinçe, Levent Subaşı, Ceyda Şanlı, Murat Taş, Sefaattin Tongay, Cem M. Turgut, Turgut Tut, Onur Umurcalılar, Hasan Yıldırım, Hatice Yılmaz.

I also present my love to my high school friends Erhan Akay and Cem Demirel, who had serious impact on me and preserve their special positions.

I got most of the motivational support from my wife Dilek Işık Taşgın during the research and the composition of this thesis. I owe her lots of my things, especially the discipline of studying.

I am grateful to my father Ahmet Taşgın, who tried a lot to keep the track of my studies with many questions, even though he didn't have knowledge on physics.

Last, I am thankful to my mother Hacer Taşgın for her support in my whole studentship life. She has even learned English with/for me in the preparatory part of the high school.

Contents

List of Figures

List of Tables

Chapter 1

Introduction

Bose-Einstein condensate (BEC) is a coherent media, which displays the collective phenomena in both internal (electronic) and center of mass motion states of its constituents. The former one is the sequential Superradiance (SR), where the incident laser pulse recoils the atoms in groups. The latter one is the Superfluidity (SF), where quantized vortices form as a result of collective rotational excitation.

When an axially-trapped BEC is optically pumped with a strong laser beam, it superradiates towards the ends (end-fire modes) of the cigar-shaped sample. Emission is highly directional. This gives rise to the collective recoiling of group of bosons to a single momentum mode (side mode). As well, the inter-atomic coherence is preserved. The collectively scattered boson clouds serve as new centers for higher-order (sequential) superradiance. Thus, a fan-shaped pattern of recoiled atomic groups forms.

Recoiling of BEC atoms by incident radiation can be utilized as an effective quantum entanglement tool. At normal (linear) scattering regime; interaction provides discrete entanglement of a single atom-photon pair. In the low pump intensity limit, scattering of a photon by a single atom is favored, due to the statistical Bose enhancement. At superradiant (nonlinear) scattering regime, on the other hand, interaction provides the continuous-variable (CV) entanglement of recoiled atomic group with the emitted superradiant pulse. In this case; enhancement of CV entanglement takes place because of the wave-like behavior

of the atomic group that originates from the coherence. Therefore, coherence plays a crucial role in the establishment of both kinds of quantum entanglement.

In Chapter 2, we demonstrate the CV quantum entanglement of the two superradiant pulses that propagates in the opposite directions. The highly directional pulses belong to two opposite end-fire modes. Establishment of entanglement is based on swapping mechanism; the CV entanglement generated between side mode and end-fire mode in the first-sequence, is swapped into the CV entanglement of two end-fire modes in the second-sequence of SR. The results of Chapter 2 are mainly based on our paper [1].

The second collective phenomena, that BEC manifests, is the formation of vortices due to the cooperative circulation of bosons. This behavior originates from the coherence in the center of mass motion states of bosons. When BEC is rotated, it behaves as a single wave wherein individual atoms cannot be resolved. When the rotation frequency passes over a critical value, vortices start to form. As the rotation frequency is increased further, more and more vortices are generated. These vortices distribute themselves periodically in the bulk of BEC. They form a lattice whose type and periodicity is governed by the parameters of the BEC.

Therefore, rotating BEC can be utilized as a photonic crystal (PC) if the required index contrast can be established. A BEC photonic crystal has several advantages over the usual ones. The lattice parameter of the PC is continuously tunable via the rotation frequency. Moreover, even the lattice type can be changed by altering the interaction strength via Feshbach resonance.

Index enhancement is available through the strong coupling schemes, which relies on the constitution of the optical atomic coherence via destructive interference of the absorption paths. This type of three/four-level coherence schemes, however, display complicated dependence of the dielectric function on the frequency. Dielectric function may change sign around the index enhancement frequency. This, however, brings out the theoretical problem of distinguishing the absorption/gain region from the photonic bad gap region; for a calculated value of imaginary wave vector.

In Chapter 3, we derive the photonic bands of a triangular lattice of BEC

vortices. We adopt a Poynting vector method. This way, we manage to distinguish the band gap regions from the absorption/gain regions without requiring the time-consuming reflection/transmission simulations. The results of Chapter 3 rely on our papers [2, 3].

Chapter 2

Continuous-variable Entanglement via sequential Superradiance of a Bose-Einstein condensate

2.1 Introduction

Superradiance (SR) refers to the collective spontaneous emission of an ensemble of atoms, due to the coherence in between the radiators. When the phases of atoms cohere, multiatomic ensemble displays a macroscopic dipole moment that is proportional to the number of atoms, N. Thus, intensity of the emission is proportional to the square of the number of atoms, $\sim N^2$. This resembles the intensity of overlap of N identical waves, all have the same (or very close) phase. In a normal or stimulated radiator N atoms radiate independently, giving rise to intensity proportional to N.

Despite the earlier theoretical introduction and study of SR by Dicke [4] in 1954, its first experimental demonstration near the optical region became available in 1973 by Skribanowitz *et. al.* [5]. Development of the strong lasers allowed the rapid pump of the sufficient number of atoms to excited level. In order to be able to observe the collective radiation, pumping time must be smaller than the decoherence time (T_2) [6] of the atomic phases. Phase coherent N excited atoms can spontaneously decay to the ground state in a time $\tau_c \sim N^{-1}$ [4, 5], where subscript c refers to coherent decay. This is because, interaction of all the atoms with the common electromagnetic field (emitted mode) establishes correlations in between the atoms. In other words, as also pointed out in subsection 2.2.1, radiation path enforces the atoms to a more correlated sate. In the superradiant state, deexcitation is equally well distributed between all N atoms. This results in an emission intensity $I \approx N\hbar\omega_0/\tau_c \sim N^2$, where $N\hbar\omega_0$ is the total energy produced by the decay of N atoms.

The distinguishing feature of SR is the spontaneous induction of the atomic coherence due to the interaction of atoms with the emission mode. In other collective phenomenon, such that free induction, photon echo and self-induced transparency [7], also intensity is proportional to N^2. The phasing between the atoms, however, is established via the coherent pumping of the atoms to the excited state. In SR, on the other hand, strong pump (need not be coherent) of the atoms to the excited level is sufficient. Initial state of atomic ensemble, where

all excited, is incoherent. Atomic coherence induces in the middle of the radiation path (see Sec 2.2.1) spontaneously, while atoms return back to the ground state.

In order to be able to observe SR pump time (T_{pump}) must be smaller than the collective spontaneous decay time (τ_c), $T_{\text{pump}} < \tau_c$. On the other hand, coherent decay must occur (otherwise it is not coherent decay) in a shorter time than the atomic decoherence time (T_2) and single atom decay time (T_1), $\tau_c < T_2, T_1$. If the length of the illuminated sample (L) is relatively short, such that $\tau = L/c \ll \tau_c$, generated photons leave active medium immediately. Neither stimulated emission nor reabsorption is unimportant. If $\tau \sim \tau_c$, however, photons can be reabsorbed by the atoms giving rise to Rabi type oscillations. This type of SR is called the Oscillatory Superradiance; more than one peaks are observed [5] in the superradiant output pulse. Oscillatory SR is observed best in a ring cavity [8, 9], where generated photons remain (rotate) in the cavity. Ringing is often explained in terms of the pulse propagation effect [10], where the finite size and shape of the medium plays significant roles [11, 12].

One another feature that SR displays is the delay time (τ_D), the time interval in which the system manages to develop the SR pulse peak [7]. The fully excited atomic ensemble starts to spontaneously radiate at a rate $R \sim N/T_1$ at the beginning, $t \sim 0$. With the start of spontaneous emission, atomic correlations grow. As time passes, more and more atoms become correlated; thus giving rise to a continuous increase in the spontaneous emission rate. At the SR peak $t = \tau_D \sim \tau_c \ln N$, the spontaneous emission rate reaches the maximum value $R \sim N/\tau_c \sim N^2$.

Most distinguishing feature of SR, due to collectivity, is the strong directionality (see Sec. 2.2.2) of the outcoming radiation in the elongated samples. The coherent output radiation leaves the sample (Fig. 2.4) throughout the ends of the elongated sample. These modes of SR radiation are called the end-fire photon modes. The reason of the directionality is the occupancy of end-fire modes by larger number of atoms compared to the sideward modes, see Sec. 2.2.2.

SR occurs in many systems [13], from thermal gases of excited atoms [14] and molecules [5], quantum dots and quantum wires [15–17], to Rydberg gases

[18], and molecular nanomagnets [19]. On the other hand, however, SR in an elongated Bose-Einstein condensates (BECs) [20] displays peculiar features. Due to the cooperative nature of SR, condensate atoms ($\mathbf{p} = 0$) are scattered into higher momentum states collectively. And, because of the strong directionality of the end-fire mode radiation, atoms are scattered approximately to the same momentum mode. These are called side modes. Furthermore, atoms are recoiled to side modes phase consistently due to the collectivity. When a side mode is sufficiently occupied they also give rise to superradiant scattering and form new side modes. The resulting picture, Fig. 2.5, is a fan-like pattern of the side modes. This phenomenon, that is observed [20] only in BEC sample, is called the sequential Superradiance.

Quantum entanglement [21, 22] is the nonlocal correlations in the measurements of quantum observables which cannot be explained/tracked classically or by introduction of a hidden variable theory [23] into quantum mechanics. If two particles are quantum entangled, the choice of type of measurement (i.e. $\mathbf{S}_x$ or $\mathbf{S}_z$) performed on the first particle instantaneously effects the result of the measurement ($\mathbf{S}_z$) made on the second particle [24]. The kind of the entanglement may vary; it can be between two particles or two modes of a radiation/atomic field. Additionally, the quantum state of the two particles/modes may be inseparable in a discrete or continuous basis. The later one is called the continuous-variable (CV) quantum entanglement.

Experimental verification of CV quantum entanglement in between the two light pulses is performed for different models [25–28]. The CV entanglement of a light pulse and cold atoms [29] is also experimentally demonstrated. The basic principle behind is the two-mode squeezing [30], where two photon-photon or photon-atom modes are coupled via squeezing type Hamiltonian (see the last part of Appendix 2.9.1). CV entanglement is also shown theoretically in three-level atomic schemes [31–34].

Experimental demonstration of the quantum teleportation [35], after the theoretical expectations [36, 37], aroused great interest. CV entanglement is

adopted for quantum cryptology [38] as well as quantum computation [39–42]. Quantum computation is based upon the the transfer of the entanglement between photon-photon, atom-atom and atom-photon pairs. The need for more durable entanglement drives the research on more correlated systems.

Recently, serious efforts have been directed towards the study of quantum entanglement between condensed atoms and SR light pulses [43–45] and entanglement between atoms through SR [15]. Several promising applications, including prospect for quantum teleportation in entangled quantum dots via SR, are proposed [15]. On the other hand, Refs. [15, 43–45] deal with different kinds of entanglements. Ref. [43] investigates the entanglement of the hyperfine states of atoms with the polarization states of the end-fire photons, via Raman SR. In Refs. [44, 45] the separability of the number basis of the end-fire and side modes is tested in Rayleigh SR. In Ref. [15] internal states of two atoms are entangled. Thus, only the atom-photon entanglements in [44, 45] are continuous variable in its nature, since the number basis of photon-atom modes are inseparable.

More recently, the Kapitza-Dirac regime of SR was observed [46] in short pulse pump scheme. Momentum side modes display X-shaped pattern, rather than a fan-like pattern of longer pulse pump regime [20]. Only in short time intervals backscattering of side modes are observable, since energy is not conserved in the occupation of these modes. In this regime, it is predicted that SR pulses must contain quantum entangled counter-propagating photons from the end-fire modes [47]. It is proposed that quantum entanglement arises from the four-wave mixing of two atomic fields (forward and backward scattered side modes) with the two photonic fields (counter-propagating end-fire modes) [47]. The predicted form of interaction, containing the terms of two-mode squeezing, suggests a CV entanglement in between the end-fire modes.

In this chapter we demonstrate the continuous-variable (CV) quantum entanglement of the two end-fire modes, during the sequential SR, even for a continuous-wave pumped condensate [20]. The origins of the photon-photon entanglement within the fan-like pattern, however, is quite different than the predicted one (four-wave mixing) within the X-shaped pattern [46, 47].

The atom-photon entanglement generated in the first sequence of SR is *swapped* into the photon-photon entanglement in the second sequence. This is because; the side mode interacted with the rightward-propagating end-fire mode in the first sequence, interacts with the leftward-propagating end-fire mode in the second sequence. In other words, counter-propagating end-fire modes are entangled due to the interaction with the same side mode, at different times. In quantum information language, entanglement is swap is a technique to entangle particles that never before interacted [48–51]. We clearly identify the swapping of the entanglement in between the two pairs (atom-photon and photon-photon) in both of our analytical and computational results.

Additionally, the form of the SR entanglement is different than the usual ones [25–29] that rely on two-mode squeezing in its constitution. In sequential SR entanglement is generated collectively and coherently, independent of the initial coherence/incoherence of the exciting pulse.

Previous studies on SR from an atomic gas have displayed multiple pulses or ringing effects [5], especially among dense atomic samples. Ringing is often explained in terms of the pulse propagation effect [10], where the finite size and shape of the medium plays significant roles [11, 12]. Adopting semi-classical theories, detailed modelling of SR from atomic condensates have been very successful, essentially capable of explaining both spatial and temporal evolutions of atomic and optical fields [52–55].

The semi-classical treatments, however, can account neither for the influence on sequential scattering associated with ring from side mode patterns nor for quantum correlations between end-fire modes. Therefore, in our treatment of entanglement we rely on a full second-quantized effective Hamiltonian, where either pump photons are dealt quantum mechanically.

The Einstein-Podolsky-Rosen (EPR)-type [23, 56] quantum correlations between end-fire modes that we investigate in this chapter, can be detected with well-known methods [57, 58] developed for CV entanglement in down-converted two-photon systems. Equivalent momentum and position quadrature variables are to be employed as observables.

This chapter is organized as follows. In sec. 2.2 we introduce the basic concepts in Superradiance, such that the collective and coherent nature of the emission, the directionality and the ringing in the pulse. Afterwards, we describe the sequential SR which occurs in the strongly optical pumped BECs. We give and drive the related system parameters of the experiment [20] which are of concern here.

In sec. 2.3, we identify the various approximations and derive the full second quantized effective Hamiltonian. In sec. 2.4, we make an extended review of the inseparability and entanglement concepts in general. We describe the criteria for continuous variable entanglement, with which we confirm the existence of quantum correlation between SR photons from the end-fire modes.

In sec. 2.5, we analytically solve the effective Hamiltonian under parametric and steady state approximations. We clearly identify the swap mechanism, and intuitively explain the steps involved for the model Hamiltonian to generate EPR pairs out of non-interacting photons. This represents the key result for this article.

In sec. 2.6, we describe the method of our numerical calculations under a proper decorrelation approximation. The results are presented in sec. 3.4, where we first examine the temporal dynamics of the entanglement in connection with the accompanying field and atomic populations. This helps to illustrate the swap of atom-photon entanglement to the photon-photon entanglement. We then study carefully this swap effect, introduce the effect of decoherence, and consider the effect of SR initialization from a two-mode squeezed vacuum and the dependence on the increase/decrease of number of atoms. Sec. 2.8 contains our conclusion.

2.2 Superradiance

The first theoretical treatment of Superradiance (SR) is made by Dicke [4] in 1954, before it is observed experimentally [5] in 1973. Many features of SR, such as collectiveness and strong directionality, can be explained by the early treatment of Dicke. He showed that the mutual coupling of atoms, through over the emitted radiation field, establishes the coherence in between these atoms. The radiation

of the coherent atoms is proportional to N^2. Initial coherence of the pump is not a necessity for SR. The strongness of the pump is sufficient. This is because; when all of the atoms are placed to the excited state, the path of the radiation (over the N-atom states) drives (enforces) the atomic system to a coherent state.

In this section, we first introduce (Sec. 2.2.1) the collective Dicke states [4], where the state of the atomic group is expressed as linear superposition of N two-level atoms. This simple treatment describes well the dynamical behavior of SR; such as the temporal width of the pulse, logarithmic dependence of the delay time and the ringing of the pulse [5]. Second, the spatial dependence is introduced (Sec. 2.2.2) into the simple Dicke-states, that well describes the directionality of the SR through the end-fire modes. Third, we introduce the sequential SR (Sec. 2.2.3) which takes place if the illuminated sample is a BEC. At last (Sec. 2.2.4), we give and drive the system parameters specific to the sequential SR experiment [20].

2.2.1 Dicke-states

The excitation (electronic) states of a group of N identical two-level atoms can be mapped to the total spin basis of N spin-1/2 particles. The Hamiltonian is

$$\hat{H}_0 = \hat{H}_{CM} + E\hat{R}_z, \tag{2.1}$$

where E is the energy level spacing. Operators $\hat{R}_q = \sum_{j=1}^{N} \hat{R}_{jq}$ $(q = x, y, z)$, are the total spin operators, where $\hat{R}_z = \sum_{j=1}^{N} \hat{R}_{jz}$ corresponds to the total excitation energy of the system. $\hat{H}_{CM}$ is the part of the Hamiltonian governing the center of mass (CM) motion of the atoms, that is separable from the electronic structure. When the spatial extent of the atoms is much less that the radiation wavelength $(L \ll \lambda)$, atom-field interaction can be written in the form of

$$\hat{H}_{af} = -\mathbf{A}(0) \cdot (\mathbf{e}_x \hat{R}_x + \mathbf{e}_y \hat{R}_y) \tag{2.2}$$

within the rotating wave approximation, where $\mathbf{e}_x$, $\mathbf{e}_y$ are real dipole-coupling vectors in the proper dimensions. Since $\hat{H} = \hat{H}_0 + \hat{H}_{af}$ commutes with $\hat{R}^2 =$

$\hat{R}_x^2 + \hat{R}_y^2 + \hat{R}_z^2$, stationary states are eigenstates of $\hat{R}^2$. Therefore, act of operators $\hat{H}$ and $\hat{R}^2$ results

$$\hat{H}\psi_{Crm} = (E_g + mE)\psi_{Crm} \quad \text{and} \quad \hat{R}^2\psi_{Crm} = r(r+1)\psi_{Crm} \tag{2.3}$$

where E_g is the ground state energy and subscript C represents the CM state. r is called as the cooperation number. State $|r, m\rangle$ is the linear combination of N atomic states such that $|++-+-\ldots\rangle$, where $\pm$ represents the upper/lower electronic level.

Matrix elements of the interaction energy $\hat{H}_{af}$ are

$$\langle C, r, m|\mathbf{e}_x\hat{R}_x + \mathbf{e}_y\hat{R}_y|C, r, m \pm 1\rangle = \frac{1}{2}(\mathbf{e}_x + i\mathbf{e}_y)\left[(r \pm m)(r \mp m + 1)\right]^{1/2}, \tag{2.4}$$

apart from a constant factor. Since the transition rates are proportional to the square of elements, the intensities become

$$I = I_0(r + m)(r - m + 1) \tag{2.5}$$

for the spontaneous radiation of the atomic ensemble.

When the sample has been illuminated with a strong pump, regardless of its coherence, all N atoms are initially pumped to the excited state. This state, where all atoms are in the excited state, is $|r = N/2, m = N/2\rangle = |++\cdots+\rangle$. On the other hand, since $\hat{H}_{af}$ commutes with $\hat{R}^2$, $\Delta r = 0$. Thus, when the system is placed in a state with cooperation number r, it remains in the the group of states with r. Therefore, being pumped to the most-excited state $|r = N/2, m = N/2\rangle$ *enforces* the system to move along a path of spontaneous radiation depicted in the first column of Fig. 2.1. The intensities of the radiation, resulting from the matrix elements (2.4), are also indicated in Fig. 2.1.

SR pulse shape

System initially ($|r = N/2, m = N/2\rangle$) makes normal spontaneous emission with intensity $I_{N/2,N/2} = NI_0$. As the m number decreases, however, spontaneous emission intensity increases up to a maximum rate $I_{N/2,0} = \frac{1}{2}\left(\frac{1}{2}N + 1\right)I_0$, where

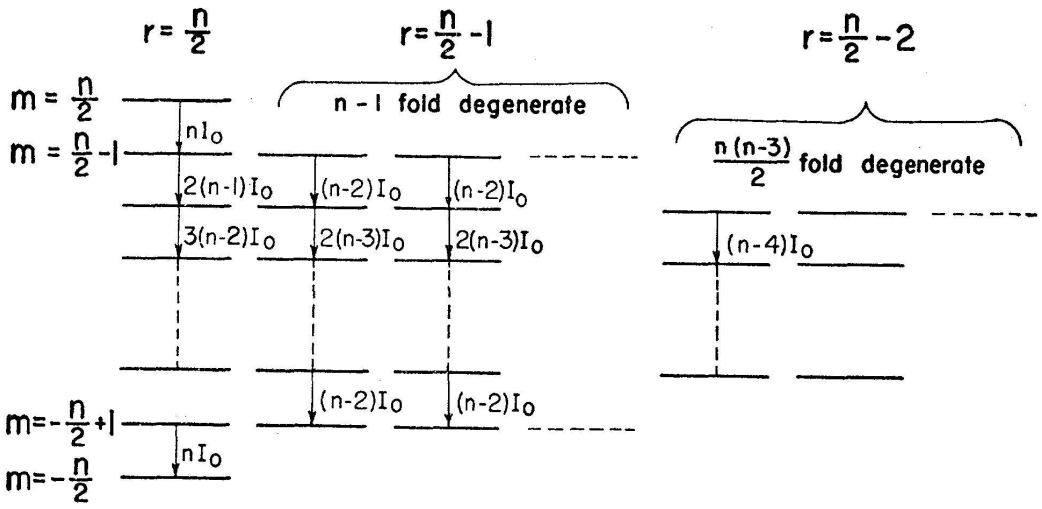

Figure 2.1: Collective N-atom ($n \equiv N$) Dicke-states; r is the cooperation number, m is the state level. First column corresponds to the radiation path of full excited system. Radiation rates are also indicated. Figure is from Ref. [4].

the occupied N atom state is $|r = N/2, m = 0\rangle$. At this state the spontaneous emission intensity is proportional to N^2, where superradiant collective scattering of atoms takes place. Further decrease in the m number results in the symmetrical decrease of the intensity to $I_{N/2,-N/2} = NI_0$, at the ground state $|r = N/2, m = -N/2\rangle$. The resulting intensity behavior [7] is depicted in Fig. 2.2.

In a second configuration, that is what happens in the experiment [20], system is initially prepared in its ground state $|r = N/2, m = -N/2\rangle = |---\cdots--\rangle$. The strong pump, again need not be coherent, continuously pumps the system up to its more excited states. While being pumped up, at the same time, excited system spontaneously radiate according to according to $I = (r+m)(r-m+1)I_0$. This continues so on until the decay rate of atoms $\sim (r+m)(r-m+1)$ exceeds the pump rate. Thereafter spontaneous emission intensity starts to decrease (almost symmetrically) till ground state is returned.

In both configurations, independent of the feature of the pump, atomic system is driven in to the more coherent state where spontaneous emission takes place collectively. Superradiant process, whose rough time dependence can be

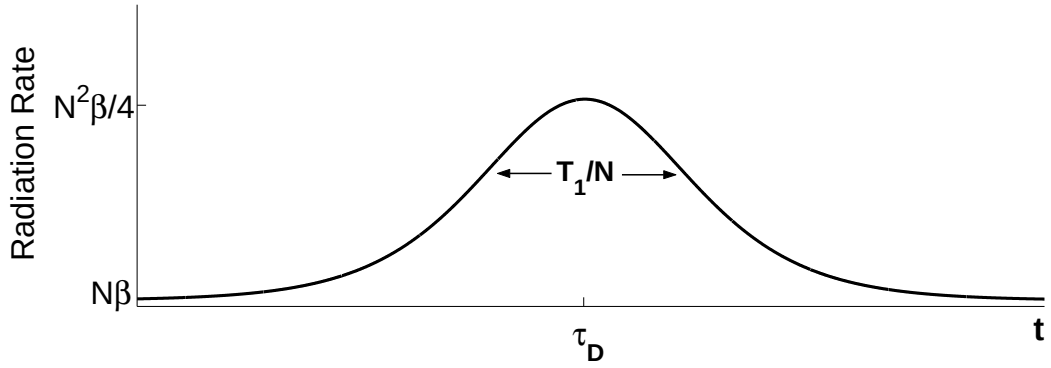

Figure 2.2: The general pulse shape of the Superradiant radiation. Normal spontaneous emission rate $R = N\beta$ at $t = 0$ (state $|r = N/2, m = N/2\rangle$) gradually evolves to Superradiant emission $R = N^2\beta/4$ (state $|r = N/2, m = 0\rangle$, $t = \tau_D \approx \ln N\tau_c$). Emission rate returns to normal $N\beta$ at $t \simeq 2\tau_D$ when system reaches the ground $|r = N/2, m = -N/2\rangle$. $\beta = 1/T_1$ is the decay rate of single atom.

approximated [7] with the rate $R(t) = \frac{N^2}{4T_1}\text{sech}^2\left(\frac{N}{2T_1}(t-\tau_D)\right)$, takes place in a narrow time width $\Delta t \simeq \tau_c = T_1/N$.

Pulse delay time

The logarithmic dependence of the pulse delay time $\tau_D \sim \tau_c \ln N$ can be derived from the following simple consideration. Simply, the integration of the inverse of the decay rates yields the correct result

$$\tau_D = \int_{m=0}^{r} dm \frac{T_1}{(r+m)(r-m+1)} = \frac{\ln(r+1)+\ln(2)}{2r+1}T_1 \approx \frac{\ln N}{N}T_1 = \tau_c \ln N, \tag{2.6}$$

where T_1 is the lifetime of the excited level for single atom. We used $N/2+1 \approx N/2$ for $N \gg 1$.

Ringing

When the length of the sample is long enough ($\tau = L/c \sim \tau_c$); the generated photons through SR do not leave the medium and re-excite the atoms to excited states. This gives rise to Rabi-like oscillations (see Fig. 2.3), which are observed

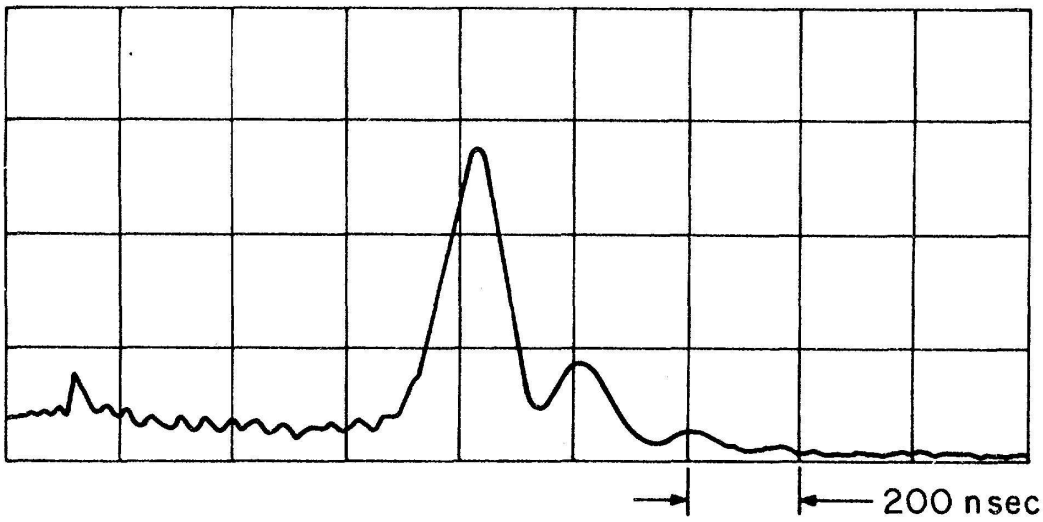

Figure 2.3: Superradiant pulse observed in the first experiment of SR near the optical region by Skribanowitz *et al.* [5]. Ringing in the pulse is due to reabsorption of the emitted photons before they left the sample. Escape time is similar to the collective radiation time; $\tau = L/c = 3\text{ns} \sim \tau_c = 6\text{ns}$.

in the experiment [5] as rings of SR pulse peaks [59].

On the other hand, the second configuration (mentioned in the subsection *SR pulse shape*) brings forward another scheme for the oscillatory SR, other than the Rabi-like one. If the pump is really strong, pumping rate may exceed the SR rate $1/\tau_c$ even though all of the atoms in the vicinity of the laser beam contributes the radiation. Thus, atoms are further pumped over the $|r = N/2, m = 0\rangle$ state, after which the spontaneous emission intensity (2.5) decreases. When the atoms are pumped up to the most-excited state $|r = N/2, m = N/2\rangle$ emission intensity becomes small. If the pump pulse is further strong, system at the most-excited state for a while (τ_W) radiating normal spontaneous emission. When the system decays, it exhibits a second peak, $t_W + 2\tau_D$ later from the first peak. This second peak is related with the first configuration mentioned above.

Therefore, for very strong pump pulse oscillatory SR takes place independent of the length of the sample or the condition $\tau \gtrsim \tau_c$. In this type there can occur at most two peaks, if Rabi-like oscillations do not contribute.

It is to be noted that the emission intensities discussed here are not to be directly compared with the ones introduced in the sections 2.4, 2.5 and 3.4. The time derivatives of the later ones give the emission intensities, since they are introduced as the occupation of the photon modes.

2.2.2 Directionality

Dynamical behavior of SR can be treated consistently with small extent gas approximation 2.2. The demonstration of the directionality of the emitted pulse, however, needs the introduction of the Dicke [4] states with spatial extent.

Interaction Hamiltonian takes the form

$$\hat{H}_{af} = -\frac{1}{2}\sum_{\mathbf{k}} \varepsilon_{\mathbf{k}} \cdot (\mathbf{e}_x - i\mathbf{e}_y)\hat{a}_{\mathbf{k}} \sum_{j=1}^{N} \hat{R}_{j+} e^{i\mathbf{k}\cdot\mathbf{r}_j} \quad + \quad H.c. \tag{2.7}$$

when the vector potential $\mathbf{A}(\mathbf{r}) = \sum_{\mathbf{k}} \left(\varepsilon_{\mathbf{k}} e^{i\mathbf{k}\cdot\mathbf{r}} \hat{a}_{\mathbf{k}} + H.c.\right)$ is placed in, where $\hat{a}_{\mathbf{k}}$ is operator annihilating one photon of momentum $\mathbf{k}$ and $\varepsilon_{\mathbf{k}}$ is the polarization vector of this photon in proper dimensions. $\mathbf{r}_j$ is the position of the j^{th} atom. $\hat{R}_{j\pm} = \hat{R}_{jx} \pm i\hat{R}_{jy}$ are the raising/lowering operators, which excites/deexcites the j^{th} atom. Introduction of the cooperative operators [4] with spatial variations

$$\hat{R}_{\mathbf{k}\pm} = \sum_{j=1}^{N} \hat{R}_{j\pm} e^{\pm i\mathbf{k}\cdot\mathbf{r}_j} \tag{2.8}$$

simplifies the interaction Hamiltonian (2.7) as

$$\hat{H}_{af} = -\frac{1}{2}\sum_{\mathbf{k}} \left[(\varepsilon_{\mathbf{k}} \cdot \mathbf{e})\hat{a}_{\mathbf{k}} \hat{R}_{\mathbf{k}+} + (\varepsilon_{\mathbf{k}} \cdot \mathbf{e})^* \hat{a}^{\dagger}_{\mathbf{k}} \hat{R}_{\mathbf{k}-}\right], \tag{2.9}$$

where $\mathbf{e} = \mathbf{k}_x - i\mathbf{k}_y$. Operator $\hat{R}_{\mathbf{k}\pm}$ excites/deexcites a collective mode where all N atoms contributes at their positions $\mathbf{r}_j$, which creates a cooperative atomic wave of upper/lower state atoms. In (2.9) creation of such an atomic wave (quasi-particle) is followed by the annihilation of a photon of momentum $\mathbf{k}$.

Hamiltonian (2.9) commutes with the total spin operator (mapping again) $\hat{R}^2_{\mathbf{k}} = \hat{R}^2_{\mathbf{k}x} + \hat{R}^2_{\mathbf{k}y} + \hat{R}^2_z$ associated with each $\mathbf{k}$. Thus, the stationary states are

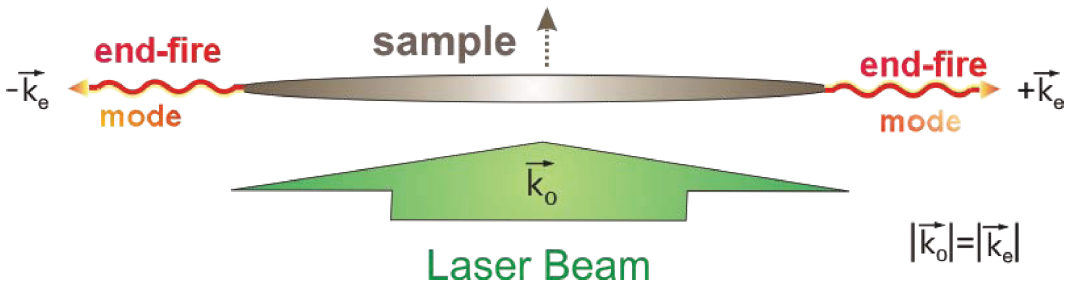

Figure 2.4: (Color online) The strong directional scattering of Superradiant pulse from an elongated sample. The scattered photons leave the sample thorough out the ends; thus these two mode $\pm\mathbf{k}_e$ are called *end-fire* modes.

eigenstates of $\hat{R}^2_{\mathbf{k}}$ with eigenvalue equation $\hat{R}^2_{\mathbf{k}}\psi_{r_{\mathbf{k}}m_{\mathbf{k}}} = r_{\mathbf{k}}(r_{\mathbf{k}}+1)\psi_{r_{\mathbf{k}}m_{\mathbf{k}}}$. Operator $\hat{R}_z = \sum_{j=1}^{N}\hat{R}_{jz}$ again exposes the eigenvalue $E\hat{R}_z\psi_{r_{\mathbf{k}}m_{\mathbf{k}}} = m_{\mathbf{k}}E\psi_{r_{\mathbf{k}}m_{\mathbf{k}}}$. Similarly, due to the commutation, $\Delta r_{\mathbf{k}} = 0$. Spontaneous emission radiation is restricted to $r_{\mathbf{k}} = N/2$ whether the system is initially in the most-excited state or the most-ground state. Therefore; similar arguments, discussed in the subsection 2.2.1, also follows here when the dynamical behavior is considered.

The directionality argument follows from the wavy Dicke states introduced by the operators $\hat{R}_{\mathbf{k}\pm}$ in (2.8). $\hat{R}_{\mathbf{k}+}$ induces an atomic wave in the $\mathbf{k}$ direction. An elongated sample illuminated perpendicular to the long axis (of length L) is to be assumed, see Fig. 2.4. Two orthogonal wave vectors $\mathbf{k}_L$ and $\mathbf{k}_W$ are to be considered, where $\mathbf{k}_L$ is in the direction of the long axis and $\mathbf{k}_W$ is in the direction of the short axis (of length W). Their magnitudes are approximately equal $|\mathbf{k}_L| = |\mathbf{k}_W| = |\mathbf{k}_0| = \omega_0/c$ due to the energy conservation. since the atomic wave created by the $\mathbf{k}_L$ is established by a larger number of atoms (about $\sim L/W$), the SR of this mode will be stronger (by $\sim (L/W)^2$ times) than the SR pulse in the direction of short axis, $\mathbf{k}_W$. Therefore, the superradiant emission is highly directional through the end-fire modes.

2.2.3 Sequential Superradiance

The collective nature of SR is exhibited more, if the illuminated sample is an elongated BEC [20]. Bosonic atoms, scattered together in the narrow time

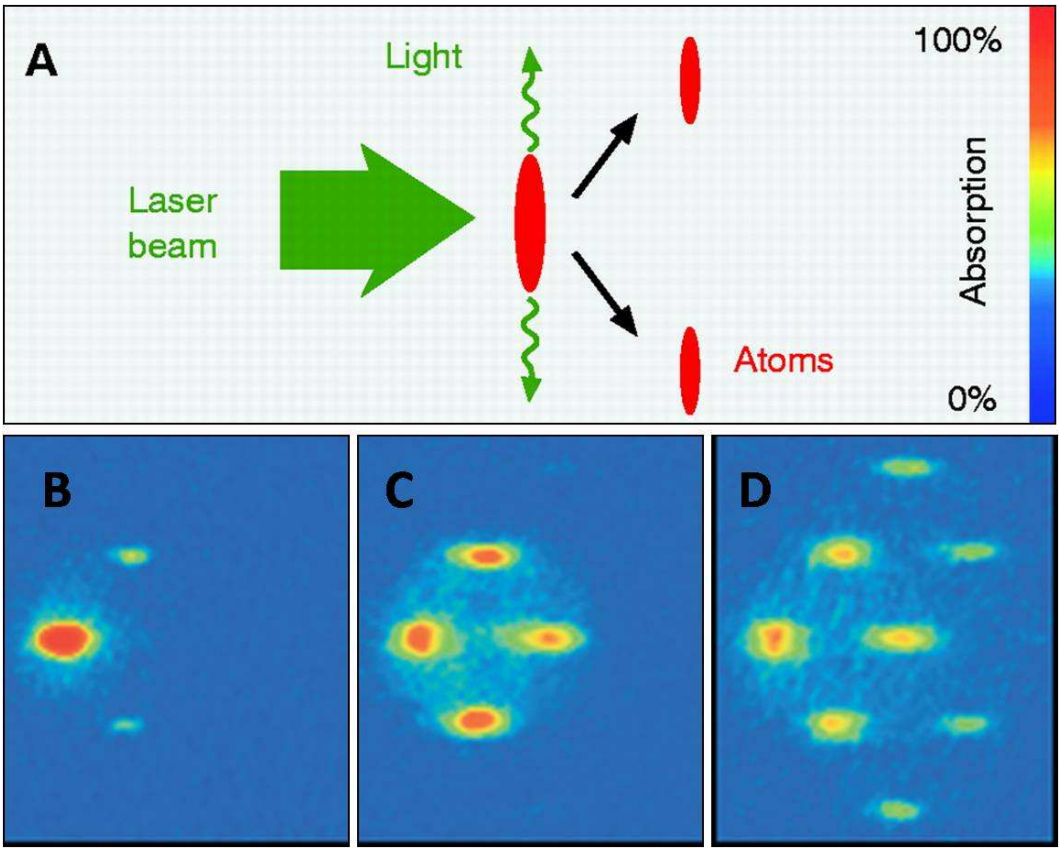

Figure 2.5: (Color online) (a) A cigar shaped BEC is illuminated with strong laser pulses of durations (b) 35μs, (c) 75μs, and (d) 100μs. Experiment is performed by Ketterle's group [20]. Absorption images show the momentum distribution of the recoiled atoms. Cooperative emission of atoms thorough out the end-fire modes results to collective scattering of the atomic groups.

interval $\Delta t \approx \tau_c$, form coherent groups (see Figs. 2.5 and 2.6) in the momentum space. Scattered groups display a fan-like pattern that is periodic in this space.

For an elongated radiating sample, such as the condensate along the z-axis being discussed here, superradiant emission occurs dominantly along the $\pm\hat{z}$ directions, *i.e.*, emitted photons leaving the cigar shaped sample mainly from both ends as depicted in Figs. 2.4 and 2.6. The corresponding spatial modes are called end-fire modes. They are perpendicular to the propagation direction of the pump laser beam. Due to momentum conservation for individual scattering events, the emission of an end-fire photon is accompanied by collective recoils of

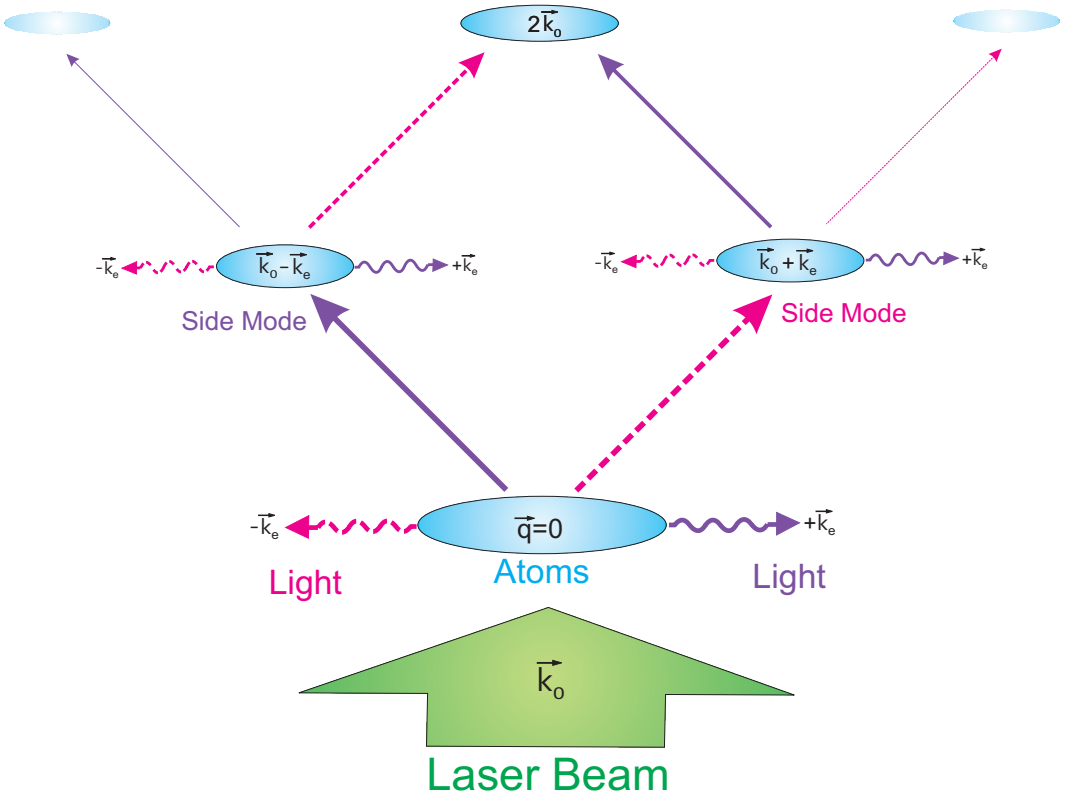

Figure 2.6: (Color online) A fan-like atomic side mode pattern up to second order sequential superradiant scattering.

the condensate atoms. The momentum of recoiled atoms is significantly larger in magnitude than the residue momentum spread of the trapped condensate.

Thus, collective recoil gives rise to distinct condensate components clearly observable in the free expansion images. These are the so-called condensate side modes. When the side modes are occupied significantly, they serve as new sources for higher order SR, or sequential SR. They, too, emit end-fire mode photons and contribute to the next order side modes. The resulting pattern for atomic distribution after expansion, as shown in Figs. 2.5 and 2.6, corresponds to what was observed for a certain choice of pump power and duration in the first BEC SR experiment [20]. The directions of the emitted end–fire mode photons and the corresponding recoiled side mode condensate bosons are indicated with the same line type.

In the earliest times, relatively small number of atoms will be recoiled by emission in comparison to condensate atoms. In this so called linear regime [44, 60–62], dynamical equations can be linearized assuming time independent, macroscopic number of condensate atoms. As the condensate atoms are depleted while more and more atoms are recoiled into other momentum states after emission, such a linearization can no longer be done. The atom-optical system then evolves according to general, coupled nonlinear equations. The linear regime is where the initiation of a superradiant pulse happens due to vacuum-field or medium fluctuations [61]. Due to their small number, recoiled atoms and emitted photons are treated quantum mechanically and it is revealed that the initial uncorrelated atom and field states get entangled as a result of simultaneous creation of recoiled atoms and associated superradiant photons [44].

The subsequent development of dynamics in the nonlinear regime leads to fully developed SR pulse which eventually decays in a final dynamical stage. At the peak of SR, the collective radiation time of the system $\tau_c \sim 10^{-3} T_1 \sim 10^{-11}$ s, becomes much smaller than the normal spontaneous emission time $T_1 = 16$ ns for typical systems. A full rigorous and detailed quantum mechanical treatment investigations of quantum correlations among atoms and emitted photons are not available for the regimes beyond the initial linear regime of SR.

2.2.4 System Parameters

This chapter, we consider a cigar shaped BEC, of length $L = 200$ μm and width $W = 20$ μm [20], that is axially symmetric with respect to the long direction of the z-axis. It is optically excited with strong laser pulse of frequency $\omega_0 = (2\pi)\times 0.508$ PHz (PHz= 10^{15} Hz) corresponding to wavelength $\lambda_0 = 589$ nm, detuned from the atomic resonance frequency ω_A by $\Delta = \omega_A - \omega_0 = 1.7$ GHz. The laser beam is directed along the y-axis, perpendicular to the long axis of the cigar shape trapped condensate. The polarization of the laser pulse is linear and along the x-direction.

The decay time of the single atom from the excited state for sodium D_2

($3^2S_{1/2} \rightarrow 3^2P_{3/2}$) line is $T_1 = 16$ ns. The decoherence time calculated in the experiment [20] is $T_2 = 62$ μs. Produced end-fire mode photons leave the BEC sample in a time of $\tau = L/c = 6.7 \times 10^{-13}$ s. And decay time of the collective spontaneous emission [59] is $\tau_c = \left(\frac{1}{4\pi\epsilon_0}\frac{2\pi N d^2 \omega_0}{V}\right) \simeq 10^{-11}$ s, where $V = LW^2$ is the effective volume of the sample and $N = 8 \times 10^6$ is the number of Sodium atoms.

Therefore, the system is in the SR regime [59]

$$\tau \ll \tau_c \ll T_1, T_2 \quad , \tag{2.10}$$

where condition $\tau \ll \tau_c$ indicated the that reabsorption of generated end-fire mode photons is negligible with high accuracy. Since τ is very small, end-fire mode photons leave the sample without feedback. This implies that Rabi-like ringing does not take place in this experiment [20].

The Rabi frequency of the pump pulse can be calculated [44] to be $\Omega_0 = \left(\frac{2d^2 I_0}{\hbar^2 \epsilon_0 c}\right)^{1/2} \simeq 0.1$ GHz, where $I_0 = 15$ mW/cm^2 is the pulse peak intensity. The approximate number of pump photons is $M \simeq I_0(LW)\tau_p/\hbar\omega_0 \simeq 2 \times 10^8$, where $\tau_p = 75$ μs is the pulse duration and (LW) is the area of the sample perpendicular to the pulse.

Since $M \gg N$, on the other hand, pumping rate exceeds the collective decay rate $\sim 1/\tau_c$. It is to be noted that; at the collective spontaneous emission region ($m \approx 0$), since factor (2.4) is common for stimulated absorption, pump photons excite the atoms also collectively. Therefore, in the experiment [20] ringing in SR pulse can be observed only due to the strong pump limit mentioned in the *Ringing* part of Sec. 2.2.1. In this ringing type there occur at most two peaks in the output superradiant pulse.

2.3 Effective Hamiltonian

In this section, we derive the effective second-quantized Hamiltonian governing the dynamics of sequential SR system. In difference to second-quantized treatments originating from Ref. [44], we treat the optical fields also quantum

mechanically. This is because; we don't want to miss any possible entanglement swap due to the interaction of the side modes with the common photonic fields. Since there exists a large energy scale difference between the center of mass (CM) dynamics for the atoms (∼MHz) and the internal electronic degree of freedom (∼PHz), we can treat their respective motions separately [63–65]. Thus the Hamiltonian of an atomic condensate with two-level atoms interacting with a near-resonant laser pump takes the following form

$$\begin{aligned}\hat{H} &= \int d^3\mathbf{r}\hat{\psi}_g^\dagger(\mathbf{r})\left(-\frac{\hbar^2}{2m}\nabla^2 + V_{\rm tg}(\mathbf{r})\right)\hat{\psi}_g(\mathbf{r}) \\ &+ \int d^3\mathbf{r}\hat{\psi}_e^\dagger(\mathbf{r})\left(-\frac{\hbar^2}{2m}\nabla^2 + V_{\rm te}(\mathbf{r}) + \hbar\Delta\right)\hat{\psi}_e(\mathbf{r}) \\ &+ \int d^3\mathbf{k}\hbar\omega_k\hat{a}_\mathbf{k}^\dagger\hat{a}_\mathbf{k} + \int d^3\mathbf{r}d^3\mathbf{k}\left[\hbar g^*(\mathbf{k})e^{-i\mathbf{k}\cdot\mathbf{r}}\hat{\psi}_g^\dagger(\mathbf{r})\hat{a}_\mathbf{k}^\dagger\hat{\psi}_e(\mathbf{r}) + \text{H.c.}\right], \quad (2.11)\end{aligned}$$

under the dipole approximation. We excluded the term $\hat{\psi}_g^\dagger\hat{a}_\mathbf{k}\hat{\psi}_e$ an its *H.c.* due to the rotating wave approximation. Since a polarized laser is used in the experiment, the incoming and outgoing pulses are going to be single polarization. Therefore, we omitted the polarization in (2.11).

The first two terms in (2.11), ($\hat{H}_{0g}$ and $\hat{H}_{0e}$), are the atomic Hamiltonians for the CM motion in their respective trapping potentials $[V_{tg}(\mathbf{r}), V_{eg}(\mathbf{r})]$ of the ground/excited internal states. Energy of the ground and excited states are taken as 0 and $\hbar\omega_A$, respectively. The atomic fields, described by annihilation (creation) operator $\hat{\psi}_{g,e}(\mathbf{r})$ $\left(\hat{\psi}_{g,e}^\dagger(\mathbf{r})\right)$, obey the usual bosonic algebra. $\hat{\psi}_{g,e}(\mathbf{r})$ $\left(\hat{\psi}_{g,e}^\dagger(\mathbf{r})\right)$ annihilates/creates one bosonic atom at the position $\mathbf{r}$, in the ground/excited internal state. In the Hamiltonian (2.11), $\hat{\psi}_e^\dagger(\mathbf{r})$) is in the rotating frame defined by the pump-laser field of frequency ω_0. $\hbar\Delta = \hbar(\omega_A - \omega_0)$ is the excitation energy of the atom in the rotating frame.

The third term in (2.11), ($\hat{H}_f$), comes from the free electromagnetic field. The interaction of electromagnetic field with the bosonic field is described with the last term ($\hat{H}_{af}$). $\hat{H}_{af}$ includes both the laser and the scattered photons. The operator $\hat{a}_\mathbf{k}$ ($\hat{a}_\mathbf{k}^\dagger$) annihilates (creates) a photon with wave vector $\mathbf{k}$, polarization $\epsilon_\mathbf{k}$, and frequency $\omega_\mathbf{k} = ck - \omega_0$ (again in the rotating frame with frequency

ω_0). $g(\mathbf{k}) = [c|\mathbf{k}|d^2/2\hbar\epsilon_0(2\pi)^3]^{1/2}\,|\hat{\mathbf{k}}\times\hat{\mathbf{x}}|$ is the dipole coupling coefficient, with $\vec{d} = \langle e|\vec{r}|g\rangle$ the matrix element for the atomic dipole transition.

We disregarded the weak, nonlinear atom-atom interaction term in Hamiltonian (1). Only its effect in the density profile is considered.

2.3.1 Adiabatic approximation of the excited state

$\hat{\psi}_e(\mathbf{r})$, in (2.11), can be approximately expressed in terms of $\hat{\psi}_g(\mathbf{r})$ via adiabatic elimination in the Heisenberg equation of motion, as follows. Time evolution of $\hat{\psi}_e(\mathbf{r})$ is governed by the equation

$$i\hbar\dot{\psi}_e(\mathbf{r}) = \left[\hat{\psi}_e, \hat{H}\right] = \left(-\frac{\hbar^2}{2m}\nabla^2 + V_{\rm te}(\mathbf{r}) + \hbar\Delta\right)\hat{\psi}_e(\mathbf{r}) + \hbar\left(\int d^3\mathbf{k}\, g(\mathbf{k})e^{i\mathbf{k}\cdot\mathbf{r}}\hat{a}_{\mathbf{k}}\right)\hat{\psi}_g(\mathbf{r}). \tag{2.12}$$

First two terms (harmonic oscillator) are related with the dynamics of atoms in the trap. Typical frequency spacing can be estimated via the minimum trap length. Using $l = \sqrt{\hbar/m\omega} = 10\mu$m the energy scale of the harmonic oscillator (HO) comes out to be order $\sim 10^5$ Hz which is much less than the detunning frequency $\Delta = 1.7$ GHz. Omitting the HO term in (2.12), formal integration yields

$$\hat{\psi}_e(t) \approx \hat{\psi}_e(0)e^{-i\Delta t} - ie^{-i\Delta t}\int d^3\mathbf{k}\, g(\mathbf{k})e^{i\mathbf{k}\cdot\mathbf{r}}\int_{t'=0}^{t} dt'\hat{a}_{\mathbf{k}}(t')\hat{\psi}_g(t')e^{i\Delta t'}. \tag{2.13}$$

Since $e^{i\Delta t'}$ oscillates very rapidly with respect to $\hat{a}(t')$ and $\hat{\psi}_g(t')$, both operates can be put out of the integral, leading to equation

$$\hat{\psi}_e(t) \approx \hat{\psi}_e(0)e^{-i\Delta t} - \frac{1}{\Delta}\left(\int d^3\mathbf{k}\, g(\mathbf{k})e^{i\mathbf{k}\cdot\mathbf{r}}\hat{a}_{\mathbf{k}}(t)\right)\hat{\psi}_g(t)\left(1 - e^{-i\Delta t}\right). \tag{2.14}$$

Since the two terms, which includes $e^{-i\Delta t}$, oscillates very rapidly they display transient behavior that can be omitted. Then, adiabatic elimination leads to the excited state atomic field operator

$$\hat{\psi}_e(\mathbf{r}) \cong -\frac{1}{\Delta}\left(\int d^3\mathbf{k}\, g(\mathbf{k})e^{i\mathbf{k}\cdot\mathbf{r}}\hat{a}_{\mathbf{k}}\right)\hat{\psi}_g(\mathbf{r}), \tag{2.15}$$

which can be expressed in terms of the ground state atomic field operator. Substitution of (2.15) into $\hat{H}_{af}$ leads to

$$\hat{H}_{af} \approx -\frac{2}{\Delta}\int d^3\mathbf{r}d^3\mathbf{k}d^3\mathbf{k}' g^*(\mathbf{k})g(\mathbf{k}')e^{-i(\mathbf{k}-\mathbf{k}')\cdot\mathbf{r}}\hat{\psi}_g^\dagger(\mathbf{r})\hat{a}_\mathbf{k}^\dagger\hat{a}_{\mathbf{k}'}\hat{\psi}_g(\mathbf{r}). \tag{2.16}$$

Similarly insertion of (2.15) into the atomic Hamiltonian for CM motion of the atoms in the excite state yields

$$\hat{H}_{0e} \approx \frac{1}{\Delta^2}\int d^3\mathbf{r}d^3\mathbf{k}d^3\mathbf{k}' g^*(\mathbf{k})g(\mathbf{k}')e^{-i(\mathbf{k}-\mathbf{k}')\cdot\mathbf{r}}\left(\hat{H}_{HO}^{(e)}+\hbar\Delta\right)\hat{\psi}_g^\dagger(\mathbf{r})\hat{a}_\mathbf{k}^\dagger\hat{a}_{\mathbf{k}'}\hat{\psi}_g(\mathbf{r}) \tag{2.17}$$

where $\hat{H}_{HO}^{(e)} = -\frac{\hbar^2}{2m}\nabla^2 + V_{\mathrm{te}}(\mathbf{r})$ is the harmonic oscillator term ($\sim 10^5$Hz) and is to be neglected beside detunning $\Delta \sim 10^9$Hz, once again.

Therefore, we observe that increase in energy due to the occupation of excited state is the half of the decrease in energy due to the atom-field interaction term. Insertion of (2.16) and (2.17) yields an effective Hamiltonian

$$\begin{aligned}\hat{H} &= \int d^3\mathbf{r}\hat{\psi}_g^\dagger(\mathbf{r})\hat{H}_{HO}^{(g)}\hat{\psi}_g(\mathbf{r}) + \int d^3\mathbf{k}\hbar\omega_k\hat{a}_\mathbf{k}^\dagger\hat{a}_\mathbf{k} \\ &- \frac{\hbar}{\Delta}\int d^3\mathbf{r}d^3\mathbf{k}d^3\mathbf{k}'\tilde{g}(\mathbf{k},\mathbf{k}',\mathbf{r})\hat{\psi}_g^\dagger(\mathbf{r})\hat{a}_\mathbf{k}^\dagger\hat{a}_{\mathbf{k}'}\hat{\psi}_g(\mathbf{r}),\end{aligned} \tag{2.18}$$

with $\tilde{g}(\mathbf{k},\mathbf{k}',\mathbf{r}) = g^*(\mathbf{k})g(\mathbf{k}')\exp\left(-i(\mathbf{k}-\mathbf{k}')\cdot\mathbf{r}\right)$, proportional to the effective coupling between the absorbed and subsequently emitted photons. Here we note that, contribution of the $\hat{H}_{HO}^{(e)}$ term in $\hat{H}_{0e}$ (2.17) is of order $\frac{\Omega_0^2}{\Delta^2} \sim 10^-2$ less than the $\hat{H}_{HO}^{(g)} = -\frac{\hbar^2}{2m}\nabla^2 + V_{\mathrm{tg}}(\mathbf{r})$ term in (2.18), where Ω_0 is the Rabi frequency given in Sec. 2.2.4.

2.3.2 Quasi-mode expansion of atomic fields

Effective Hamiltonian (2.18) does not reveal the interaction between the momentum side modes of the condensate with the pump/end-fire mode photons, explicitly. Thus we expand the atomic field operator $\hat{\psi}_g(\mathbf{r})$ in terms of the quasi-particle excitations of BEC

$$\hat{\psi}_g(\mathbf{r}) = \sum_\mathbf{q}\langle\mathbf{q}|\mathbf{r}\rangle\hat{c}_\mathbf{q}, \tag{2.19}$$

as described in Ref. [62]. State $|\mathbf{q}\rangle$ corresponds to a plane wave type quasiparticle oscillation, $\langle \mathbf{r}|\mathbf{q}\rangle = \phi_0(\mathbf{r})e^{i\mathbf{q}\cdot\mathbf{r}}$, over the trapped initial condensate wave function $\phi_0(\mathbf{r})$. Since the condensate has a finite size, recoil momentum quantizes approximately as $\mathbf{q} = \hat{\mathbf{z}}n_z\frac{2\pi}{L} + (\mathbf{q}\hat{\mathbf{x}}n_x + \hat{\mathbf{y}}n_y)\frac{2\pi}{W}$, where $n_{x,y,z} = 0, 1, 2, \ldots$ all integers.

We note that, the quantization of the momentum excitations in the $\hat{\mathbf{x}}$,$\hat{\mathbf{y}}$ directions $\Delta q_{x,y} = \frac{2\pi}{W} \approx 3 \times 10^{-5}\mathrm{m}^{-1}$ is 1/30 of the momentum of the pump/end-fire mode photons $k_0 = \omega_0/c = 10^7\mathrm{m}^{-1}$. The quasimodes excitations approximately form an orthonormal basis because $\langle \mathbf{q}|\mathbf{q}'\rangle \approx \delta_{\mathbf{q}\mathbf{q}'}$. $\hat{c}_{\mathbf{q}}$ ($\hat{c}^\dagger_{\mathbf{q}}$) annihilates (creates) a scattered boson in the momentum side mode $\mathbf{q}$, and obeys the boson commutation relations $[\hat{c}_{\mathbf{q}}, \hat{c}^\dagger_{\mathbf{q}'}] = \langle \mathbf{q}|\mathbf{q}'\rangle \approx \delta_{\mathbf{q}\mathbf{q}'}$. Another approach is the expansion of atomic field operator in terms of the harmonic oscillator modes [86]. This approach is less approximate, but it is harder to track the side modes.

When we insert the expansion (2.19) into the first term ($\hat{H}_{0g}$) of (2.18) it results

$$\hat{H}_{0g} = \int d^3\mathbf{r} \sum_{\mathbf{q}} \langle \mathbf{q}|\mathbf{r}\rangle \hat{c}^\dagger_{\mathbf{q}} \hat{H}^{(g)}_{HO} \sum_{\mathbf{q}'} \langle \mathbf{r}|\mathbf{q}'\rangle \hat{c}_{\mathbf{q}'}. \tag{2.20}$$

The first-quantized $\hat{H}^{(g)}_{HO}$ operator acted on the quasimode wave function $\langle \mathbf{r}|\mathbf{q}'\rangle$ can be expressed as

$$\hat{H}^{(g)}_{HO}\langle \mathbf{R}|\mathbf{q}'\rangle = \left[\hat{H}^{(g)}_{HO}\phi_0(\mathbf{r})\right] e^{i\mathbf{q}'\cdot\mathbf{r}} + \frac{\hbar^2 q'^2}{2m}\phi_0(\mathbf{r})e^{i\mathbf{q}'\cdot\mathbf{r}} - 2\frac{\hbar^2}{2m}\left(\vec{\nabla}\phi_0(\mathbf{r})\right)\cdot\left(i\mathbf{q}'e^{i\mathbf{q}'\cdot\mathbf{r}}\right) \tag{2.21}$$

The third term in (2.21), which is of order $\frac{2\pi}{k_0 W} \sim \frac{1}{30}$ smaller compared to the second one, is to be neglected. The first term produces $\hat{H}^{(g)}_{HO}\phi_0(\mathbf{r}) = \mu\phi_0(\mathbf{r})$ from the Gross-Pitaevskii equation. On the other hand, chemical potential is very close to zero $\mu \simeq 0$ throughout the BEC regime. Therefore, in the second-quantized form within the side mode representation Hamiltonian (2.18) becomes

$$\begin{aligned}\hat{H} \quad &= \sum_{\mathbf{q}} (\mu + \hbar\omega_q)\hat{c}^\dagger_{\mathbf{q}}\hat{c}_{\mathbf{q}} + \int d^3\mathbf{k}\hbar\omega_k \hat{a}^\dagger_{\mathbf{k}}\hat{a}_{\mathbf{k}} \\ &\quad -\frac{\hbar}{\Delta}\sum_{\mathbf{q},\mathbf{q}'}\int d^3\mathbf{k}d^3\mathbf{k}' g^*(\mathbf{k})g(\mathbf{k}')\rho_{\mathbf{q},\mathbf{q}'}(\mathbf{k},\mathbf{k}')\hat{c}^\dagger_{\mathbf{q}}\hat{a}^\dagger_{\mathbf{k}}\hat{a}_{\mathbf{k}'}\hat{c}_{\mathbf{q}'},\end{aligned} \tag{2.22}$$

where $\rho_{\mathbf{q},\mathbf{q}'}(\mathbf{k},\mathbf{k}') = \int d\mathbf{r}|\phi_0(\mathbf{r})|^2 e^{i[(\mathbf{k}+\mathbf{q})-(\mathbf{k}'+\mathbf{q}')]\cdot\mathbf{r}}$ is the structure form factor of the condensate density, which is responsible for the highly directional emission of the end-fire mode photons. $\hbar\omega_{\mathbf{q}} = \hbar^2|\mathbf{q}|^2/2m$ is the side mode energy at the recoil momentum of $\mathbf{q}$.

The first two terms in Eq. (2.22) are diagonal in their respective Fock spaces and can be omitted by performing further rotating frame transformations $\hat{c}_{\mathbf{q}} \rightarrow \hat{c}_{\mathbf{q}} e^{-i(\mu/\hbar+\omega_{\mathbf{q}})t}$ and $\hat{a}_{\mathbf{k}} \rightarrow \hat{a}_{\mathbf{k}} e^{-i\omega_{\mathbf{k}}t}$. Thus, the effective Hamiltonian takes the form

$$\hat{H} = -\frac{\hbar}{\Delta}\sum_{\mathbf{q},\mathbf{q}'}\int d^3\mathbf{k}d^3\mathbf{k}' g^*(\mathbf{k})g(\mathbf{k}')\rho_{\mathbf{q},\mathbf{q}'}(\mathbf{k},\mathbf{k}')\hat{c}^\dagger_{\mathbf{q}}\hat{a}^\dagger_{\mathbf{k}}\hat{a}_{\mathbf{k}'}\hat{c}_{\mathbf{q}'}e^{i\left(\omega_{\mathbf{k}}+\omega_q-\omega_{\mathbf{k}'}-\omega_{q'}\right)t}, \quad (2.23)$$

where $\hat{a}_{\mathbf{k}}$ is in total in the frame rotating with frequency $c|\mathbf{k}|$ and $\hat{c}_{\mathbf{q}}$ is $(\mu/\hbar+\omega_{\mathbf{q}})$.

2.3.3 Single-mode Approximation

In a sufficiently elongated condensate, large off-axis Rayleigh scattering is suppressed with respect to the end-fire modes [86]. The angular distribution of the scattered light is sharply peaked at the axial directions ($\mathbf{k}_e = \pm k_e\hat{z}$), if the Fresnel number is larger than one $\mathcal{F} = W^2/L\lambda_0 \gtrsim 1$ at the pump wavelength λ_0 for a condensate of length L and width W [62]. This makes it possible to consider only the axial end-fire modes. Furthermore, the strong discretization of the side modes in the $\hat{x}$,$\hat{y}$ directions, $\Delta q_{x,y} \simeq \frac{k_0}{30}$, reinforces the single mode approximation.

To investigate sequential SR, we further take into account the first order side modes at $\mathbf{q} = \mathbf{k}_0 \pm \mathbf{k}_e$ and the second order side mode at $\mathbf{q} \approx 2\mathbf{k}_0$. The rest of the side modes are assumed to remain unpopulated [52]. This approximate model well describes the system up to a certain time, at where $q \simeq 2k_0$ mode is significantly occupied. This is because; collective nature of SR makes it a discrete phenomenon, happening in a $\delta t \simeq \tau_c$ time interval which may become small compared to $\tau_D \sim \tau_c \ln N$ (see Sec. 2.2.1). Thus, the occupation of the higher order side modes are vanishingly zero unless well loaded $q \simeq 2k_0$ mode gives rise to the third-order SR. The absorption image [20] for a 75μs pulse, pictured in Fig.2.5c, parallels the above discussion.

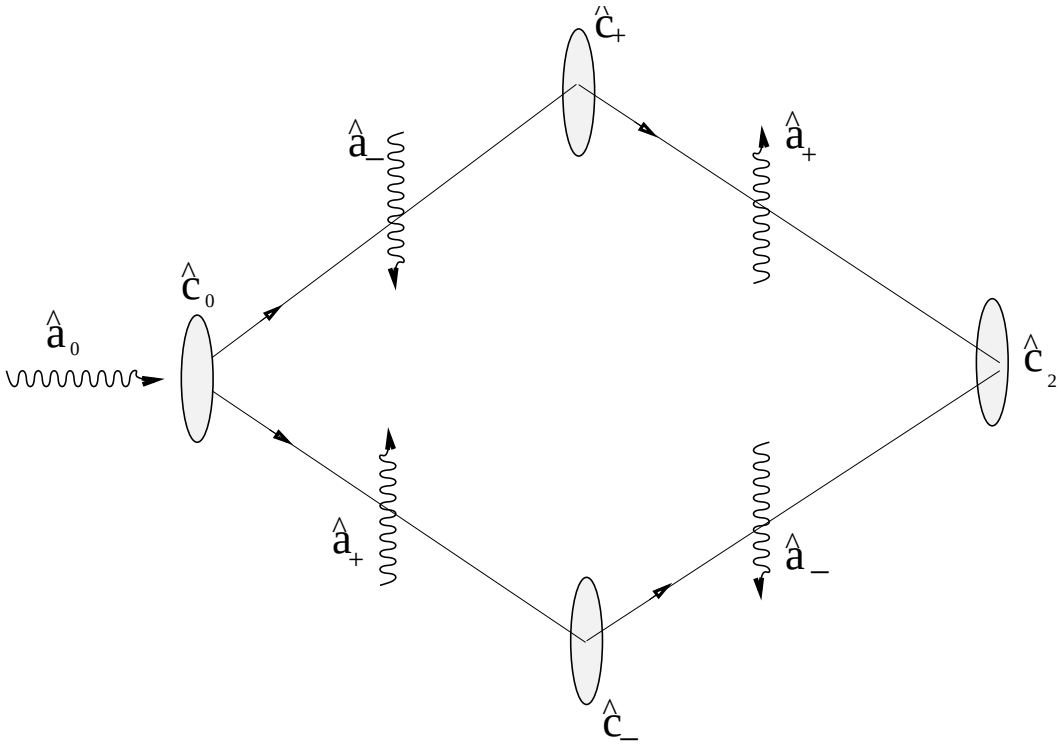

Figure 2.7: Schematic description of the roles of pump mode ($\hat{a}_0$), end-fire mode ($\hat{a}_\pm$), and side mode ($\hat{c}_0$,$\hat{c}_\pm$, and $\hat{c}_2$) annihilation/creation operators.

The Hamiltonian (2.23) that originally contains the contributions from all the side modes and the end-fire modes as well as the laser field then reduces to the following simple model:

$$\hat{H} = -\hbar\frac{g^2}{\Delta}\left(\hat{c}_+^\dagger\hat{a}_-^\dagger\hat{a}_0\hat{c}_0 + \hat{c}_-^\dagger\hat{a}_+^\dagger\hat{a}_0\hat{c}_0 + \hat{c}_2^\dagger\hat{a}_-^\dagger\hat{a}_0\hat{c}_- + \hat{c}_2^\dagger\hat{a}_+^\dagger\hat{a}_0\hat{c}_+\right) + \text{H.}c., \qquad (2.24)$$

with $g \equiv g(\mathbf{k_e})$. We have adopted a shorthand notation where $\hat{a}_\pm \equiv \hat{a}_{\pm\mathbf{k}_e}$, $\hat{a}_0 \equiv \hat{a}_{\mathbf{k}_0}$, $\hat{c}_\pm \equiv \hat{c}_{(\mathbf{k}_0\pm\mathbf{k}_e)}$, and $\hat{c}_2 \equiv \hat{c}_{2\mathbf{k}_0}$. The roles of these operators are schematically described in Fig. 2.7.

This is the model Hamiltonian involving the interplay of the four atomic side modes with three photonic modes. Before we further discuss and reveal the built-in entanglement swap mechanism for EPR-type quantum correlations in this model Hamiltonian, in the next section we shall briefly review continuous variable entanglement and extend its criteria to our case.

2.4 Criteria for Continuous Variable Entanglement

The existence of continuous variable entanglement is determined by a sufficient condition on the inseparability of continuous variable states as given in Ref. [67]. If the density matrix of a quantum system is inseparable within two well defined modes [31, 67–69], these two modes are quantum entangled. Entanglement of the two modes implies the quantum correlation in the measurements of electric/magnetic fields of the radiation over these modes.

In order to give the idea of what kind of correlations are dealt with, we make a short survey on the origins of the entanglement witness parameter below.

2.4.1 Separability of Subsystems

Two components of a quantum system are separable (only classically correlated) [69] if the density matrix can be expressed in the form

$$\rho = \sum_r p_r \; \rho_r^1 \otimes \rho_r^2 \; , \tag{2.25}$$

where $\rho_r^{1,2}$ are the density matrices describing the states of the subsystems 1,2. States of the subsystems ρ_r^1,ρ_r^2 are written in the basis (B^1,B^2) whose in between the correlations (inseparability) is tested. $\rho_r^{1,2}$ may as well be mixed states (linear combinations), as long as it is written in the predefined (fixed) basis (B^1,B^2).

p_r's are the positive statistical (classical) probabilities that the experiment (device) generates the first subsystem in the state ρ_r^1 and (together with) the second subsystem in the state ρ_r^2, at the same roll. We note that, since p_r is positive definite, within the basis transformations resulting ρ may not be able to be written in the form (2.25). Thus, separability of the two subsystems in two basis, does not imply the separability in other two basis. Index r enumerates any combinations of the pure/mixed quantum states belonging to the first and the second subsystems, as far as experimental setup is possible to produce.

On the way; the word *classically correlated* follows [69] from the inability of the factorization of the expectation values of observables $A^{1,2}$ belonging to the subsystems 1,2. Expectations of $A^{1,2}$, in the state (2.25), is written as

$$tr\left(\rho \cdot A^1 \otimes A^2\right) = \sum_r \rho_r \; tr\left(\rho_r^1 A^1\right) tr\left(\rho_r^2 A^2\right) \;, \tag{2.26}$$

which is classically correlated; if $tr\left(\rho_r^1 A^1\right)$ is observed in subsystem 1, $tr\left(\rho_r^2 A^2\right)$ has to be observed in in subsystem 2. This is to be distinguished from the quantum correlations [24], where the decision of the type of the observation on the first subsystem changes the result of the observation on the second system. This is because different observations collapse the state of the first subsystem to one of its eigenstates. In addition, the subsystems 1,2 may correspond to two modes, as well as two particles.

2.4.2 Quantum Entanglement

On the other hand, if the density matrix of a composite system cannot be expressed in the form of (2.25), then the two subsystems are quantum entangled (EPR correlated). Correlations may be over the values of a continuous variable (CV) observable, such as electric/magnetic field of photons emitted from the two modes or position/momentum quadratures of the two particles. As well, the values of a discrete variable (DV) observable, such as the $\hat{S}_{x,y,z}$, $\hat{L}_{x,y,z}$ of two electrons. The type of the correlations depends on, at which basis the system cannot be represented as (2.25).

Both inseparability and violation of Bell's inequality (that is violation of positiveness of the probabilities) arguments imply the existence of the quantum entanglement. However, Bell's inequality is more restrictive [68]. Satisfaction of the Bell's inequality does not always conclude the nonexistence of the quantum entanglement.

2.4.3 CV entanglement criteria

A test for continuous variable systems is derived in Ref. [67]. It tests the inseparability two infinite (number) spaces belonging to two different mode, over a continuous variable.

It follow that; for two entangled modes, the total variance of EPR-type operators

$$\hat{u} = |c|\hat{x}_1 + \hat{x}_2/c \quad \text{and} \quad \hat{v} = |c|\hat{p}_1 - \hat{p}_2/c \,, \tag{2.27}$$

are bounded above by inequality

$$\langle \Delta\hat{u}^2 \rangle + \langle \Delta\hat{v}^2 \rangle < \left(c^2 + 1/c^2\right) \,, \tag{2.28}$$

where $\hat{x}_{1,2} = (\hat{a}_{1,2} + \hat{a}^\dagger_{1,2})/\sqrt{2}$ and $\hat{p}_{1,2} = (\hat{a}_{1,2} - \hat{a}^\dagger_{1,2})/i\sqrt{2}$ are analogous position and momentum operators as in the case of a simple harmonic oscillator. The subindexes corresponds to mode numbers. c is a real number, whose value is chosen such that the separability condition (2.25) condition is tried to be violated.

In the derivation [67] of (2.28) the Cauchy-Schwarz inequality $\left(\sum_i p_i\right)\left(\sum_i p_i \langle u\rangle_i^2\right) \geq \left(\sum_i p_i |\langle u\rangle|\right)^2$ is used, which relies on the positivity of the probabilities p_i. Thus, separability/inseparability implication of the satisfaction/violation of (2.28) is not valid if the basis are carried out of the number basis.

We define the inseparability parameter

$$\lambda = \langle \Delta\hat{u}^2 \rangle + \langle \Delta\hat{v}^2 \rangle - \left(c^2 + 1/c^2\right) . \tag{2.29}$$

The presence of the continuous variable ($\hat{u}$,$\hat{v}$) entanglement in between the number spaces of the two modes is then characterized by the sufficient condition

$$\lambda < 0 \quad . \tag{2.30}$$

For the two modes to be quantum entangled, it suffices to find only one value of c that leads to $\lambda < 0$. Hence, c can be taken at which λ is minimum. Value of c, at the same time, determines the observable (variable) of the correlations.

On the other hand, the total variance of the EPR operators $\hat{u}$ and $\hat{v}$ are bounded below by

$$\langle \Delta \hat{u}^2 \rangle + \langle \Delta \hat{v}^2 \rangle \geq \left| c^2 - 1/c^2 \right| \ , \tag{2.31}$$

following from the Heisenberg uncertainty principle. Thus, λ has a lower bound

$$\lambda_{\text{low}} = \left| c^2 - 1/c^2 \right| - \left(c^2 + 1/c^2 \right) ; , \tag{2.32}$$

clearly always negative.

Criteria (2.30), $\lambda < 0$, can be quickly tested for EPR pairs [23] $\hat{x}_1 + \hat{x}_2$ and $\hat{p}_1 - \hat{p}_2$, where $\hat{x}_{1,2}/\hat{p}_{1,2}$, here, correspond to the position/momentum operators of two electrons. These are the operators (2.27) with $c = 1$. It is known [23, 67] that maximally entangled continuous variable state is the eigenstate of both $\hat{u} = \hat{x}_1 + \hat{x}_2$ and $\hat{v} = \hat{p}_1 - \hat{p}_2$ operators, at the same time. Since $\langle \Delta u^2 \rangle = \langle \Delta v^2 \rangle = 0$ for an eigenstate ket, parameter (2.29) is found to be negative; $\lambda = -2 = \lambda_{\text{low}}$ with $c = 1$.

The test of this criteria for physically entangled continuous variable states, the two-mode squeezed states, is also given in the last part of Appendix 2.9.1. It follows that the increase in the degree of squeezing decreases the λ parameter along the more negative values.

After minimization with respect to c, λ can be expressed more explicitly as

$$\lambda = 2 \left(c^2 \langle \hat{a}_1^\dagger \hat{a}_1 \rangle + \langle \hat{a}_2^\dagger \hat{a}_2 \rangle / c^2 + \text{sign}(c) \langle \hat{a}_1 \hat{a}_2 + \hat{a}_1^\dagger \hat{a}_2^\dagger \rangle \right) - \langle \hat{u} \rangle^2 - \langle \hat{v} \rangle^2, \tag{2.33}$$

where c is chosen to be $c^2 = \left[(\langle \hat{a}_2^\dagger \hat{a}_2 \rangle - |\langle \hat{a}_2 \rangle|^2) / (\langle \hat{a}_1^\dagger \hat{a}_1 \rangle - |\langle \hat{a}_1 \rangle|^2) \right]^{1/2}$ with sign $\text{sgn}(c) = -\text{sgn}\left[\text{Re}\left\{ \langle \hat{a}_1 \hat{a}_2 \rangle \right\} - \text{Re}\left\{ \langle \hat{a}_1 \rangle \right\} \text{Re}\left\{ \langle \hat{a}_2 \rangle \right\} + \text{Im}\left\{ \langle \hat{a}_1 \rangle \right\} \text{Im}\left\{ \langle \hat{a}_2 \rangle \right\} \right]$. Unlike other model investigations [31] of EPR-like correlations based upon λ, we need to keep track of the $\langle \hat{u} \rangle^2$ and $\langle \hat{v} \rangle^2$ terms, because $\langle \hat{x}_{1,2} \rangle$ and $\langle \hat{p}_{1,2} \rangle$ do not necessarily vanish for our model during time evolution. This is due to the presence of coherence of atoms/photons after the collective scattering. The parameter (2.33) defines a general criteria for continuous variable entanglement.

In the system we study here; we are mainly interested in the entanglement of the two end-fire modes ($|\hat{a}_1 = \hat{a}_+\rangle$,$|\hat{a}_2 = \hat{a}_-\rangle$) propagating in the $\pm\hat{z}$ directions.

Second, we are also interested in the entanglement of the end-fire mode and side mode ($|\hat{a}_1 = \hat{a}_\pm\rangle$,$|\hat{a}_2 = \hat{c}_\mp\rangle$), scattered in the opposite directions. In this case, one mode belongs to the photonic field and second mode to atomic field. Since the time evolutions of the two end-fire modes are necessarily symmetric (such as $\langle\hat{a}_+(t)\rangle = \langle\hat{a}_-(t)\rangle$, $\langle\hat{a}_+^\dagger\hat{a}_+(t)\rangle = \langle\hat{a}_-^\dagger\hat{a}_-(t)\rangle$) in our system, we find that $c^2 = 1$. This implies a lower bound, following from the Heisenberg uncertainty in (2.31), of $\lambda_{\text{low}} = -2$.

$\hat{a}_\pm$ ($\hat{a}_\pm^\dagger$) corresponds to annihilation (creation) of photons in the end-fire modes propagating in the $\pm\hat{z}$ directions. Thus; the variables, over which the the quantum correlations to be detected are Electric and Magnetic fields $\hat{E}_\pm = \epsilon(\hat{a}_\pm + \hat{a}_\pm^\dagger)$, $\hat{H}_\pm = \epsilon/v(\hat{a}_\pm - i\hat{a}_\pm^\dagger)$ at the fixed position.

It is worth nothing that; the CV entanglement defined here is not to be mixed/compared with the discrete variable (DV) entanglement discussed in Ref. [70]. In this chapter, the correlations in the electric/eagnetic fields of the photons from the two modes are investigated. Whereas, in Ref. [70], spin correlations of the photons from the two modes are researched. As mentioned earlier in Sec. 2.4.1, existence of correlations in between two basis does not imply the correlation in between the other two basis, even though basis belong to the same two modes/particles. Additionally, the correlations over one CV does not imply the correlations of the basis over another CV; i.e. the parameter (2.33) may become negative for a certain value of c and may not for another value of c, which correspond to different variables in (2.27).

In the remainder of this paper, we examine the time evolution of the continuous variable entanglement witness $\lambda(t)$ both for the opposite end-fire modes and for the end-fire modes with side modes. This study is expected to provide insight into the temporal development and the swap of quantum correlations between different sub-systems/modes. The following section is aimed at establishing an intuitive understanding of how EPR-like correlations between opposite end-fire modes are built up.

2.5 An entanglement Swap Mechanism

In sec. 3.4 we will exhibit the numerical results for the time evolution of the entanglement parameter $\lambda(t)$, governed by the Hamiltonian (2.24). We will observe that there exists regions in time where λ becomes negative, *i.e.*, conclusive evidence for the presence of entanglement during dynamical evolution. In this section, we hope to provide an intuitive understanding to support the result revealed through the numerical approach. We will show that it is due to the presence of an inherent swap mechanism which leads to the generation of the EPR photon pair. We shall examine the dynamical behavior of the system in two different time regimes, the early times when the first side modes just start to grow and the later times when the second order side mode contributes to the dynamics.

2.5.1 Early Times

In the initial stage, occupation of the second order side mode ($|c_2\rangle$) can be neglected. During this initiation period of the short-time dynamics, the number of atoms in the zero-momentum state can be assumed undepleted $\hat{c}_0 \approx \sqrt{N}e^{i\phi_1}$ with a constant N standing for the number of condensed atoms, like in the treatment of degenerate parametric processes. Since the pump is very strong, and the number of pump photons are much larger than the number of condensate atoms $M \gg N$, it can also be treated within the parametric pump approximation $\hat{a}_0 \approx \sqrt{M}e^{i\theta_0}$ as undepleted. Thus, the initial behavior of the system is governed by the Hamiltonian

$$\hat{H}_1 = -\hbar\chi_1 \left[e^{i\theta_1} \left(\hat{a}_+^\dagger \hat{c}_-^\dagger + \hat{a}_-^\dagger \hat{c}_+^\dagger \right) + \text{H.c.} \right], \tag{2.34}$$

with $\chi_1 = \sqrt{NM}|g|^2/\Delta$ and $\theta_1 = \theta_0 + \phi_1$ is the initial phases difference. This form of $\hat{H}_1$ is exactly the same as that of two uncoupled optical parametric amplifiers (OPAs). It allows for the growth of the first-order side modes [62] as well as the entanglement of side mode atoms with the end-fire mode photons [71]. The solution to $\hat{H}_1$ in the Heisenberg picture is given by the following time

dependencies of operators [7]

$$\hat{a}_{\pm}(t) = \cosh(\chi_1 t)\hat{a}_{\pm} + ie^{i\theta}\sinh(\chi_1 t)\hat{c}^{\dagger}_{\mp}, \tag{2.35}$$

$$\hat{c}_{\pm}(t) = \cosh(\chi_1 t)\hat{c}_{\pm} + ie^{i\theta}\sinh(\chi_1 t)\hat{a}^{\dagger}_{\mp}, \tag{2.36}$$

where the operators without time arguments are at the initial time.

The side modes and the end-fire modes are initially unoccupied $|a_+, a_-, c_+, c_-\rangle = |0, 0, 0, 0\rangle$, or taken to be in their respective vacuum states. The time dependencies for the populations of the side modes and end-fire modes come out as $\langle \hat{I}_{\pm}\rangle = \langle \hat{n}_{\pm}\rangle = \sinh^2(\chi_1 t)$, the details are given in Appendix 2.9.1. These are analogous to the classical results [7]. Evaluating correlations between the two end-fire modes (e), we find

$$\lambda \equiv \lambda_{\rm ee} = 4\sinh^2(\chi_1 t), \tag{2.37}$$

which is always positive $\lambda_{\rm ee} > 0$. On the other hand, the correlation between the end-fire mode (e) and side mode (s), scattered in the opposite directions, takes the following form

$$\lambda_{\rm se} = 2\left[2\sinh^2(\chi_1 t) - |\sin(\theta_1)|\sinh(2\chi_1 t)\right], \tag{2.38}$$

which starts with $\lambda_{\rm se}(t) = 0$ and evolves down to $\lambda_{\rm se}(t_0 \gtrsim 2) \simeq -2$, the lowest possible value of $\lambda_{\rm low} = -2$ imposed by the Heisenberg uncertainty, at $|\sin(\theta_1)| \simeq 1$.

In Figs. 2.10(a) and 2.10(b), this is further supported by more elaborate results from numerical calculations of λ and $\lambda_{\rm se}$. Same conclusions can be seen for the analytical results (2.37) over the range t = 0-t = 0.3ms in Fig. 2.10(a) and (2.38) over the range t = 0-0.2ms in Fig. 2.10(b).

2.5.2 Later Times

At later times, the first-order side modes become significantly populated, giving rise to noticeable second sequence of SR from the edges of these side mode condensates. In this case, the occupancy for the $|c_0\rangle$ mode is not an important issue, but the $|c_2\rangle$ mode becomes populated due to the second order SR.

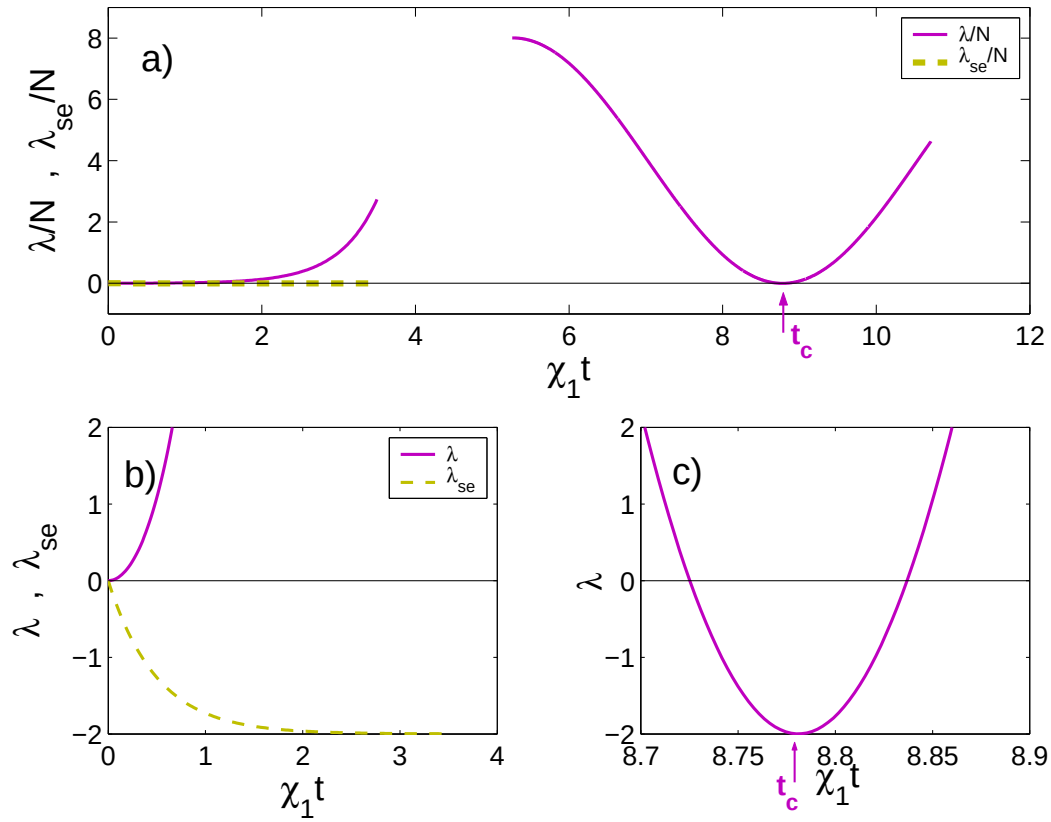

Figure 2.8: (Color online) The earlier and later times approximate behaviors of the entanglement parameters $\lambda_{\rm se}$ (between side mode and end-fire mode) and λ (between two end-fire modes). Atom-photon entanglement $\lambda_{\rm se}(t)$ at initial times is swapped into photon-photon entanglement $\lambda(t)$ at later times.

We construct an approximate model by assuming that the occupation of $|c_2\rangle$ is not changing too much, or effectively treating it as in in the steady state with $\hat{c}_2 \approx \sqrt{N_2}e^{-i\phi_2}$. N_2 is the number of atoms in the $|c_2\rangle$ state. The later stage dynamics of the system, where the 2nd order SR is effective, is then governed by the model Hamiltonian

$$\hat{H}_2 = -\hbar\chi_2 \left[e^{i\theta_2} \left(\hat{a}_-^\dagger \hat{c}_- + \hat{a}_+^\dagger \hat{c}_+ \right) + \text{H.c.} \right], \tag{2.39}$$

with $\chi_2 = \sqrt{N_2 M}|g|^2/\Delta$ and $\theta_2 = \bar{\theta}_0 + \phi_2$. As before we again neglect the depletion of the pump $\hat{a}_0 \approx \sqrt{M}e^{i\bar{\theta}_0}$.

This model $\hat{H}_2$ is also exactly solvable. The time dependencies of the annihilation operators in the Heisenberg picture are

$$\hat{a}_\pm(t) = \cos(\chi_2\Delta t)\hat{a}_\pm + ie^{i\phi_2}\sin(\chi_2\Delta t)\hat{c}_\pm, \tag{2.40}$$

$$\hat{c}_\pm(t) = \cos(\chi_2\Delta t)\hat{c}_\pm + ie^{-i\phi_2}\sin(\chi_2\Delta t)\hat{a}_\pm, \tag{2.41}$$

where $t > t_0$, the operators without time arguments are at $t = t_0$, and $\Delta t = t - t_0$. We can approximately connect these two models together into smooth temporal dynamics if we use the solutions of $\hat{H}_1$ as the initial state for dynamics due to $\hat{H}_2$ so that $\hat{a}_\pm(t_0)$ and $\hat{c}_\pm(t_0)$ are calculated at $t = t_0$ from the equations (2.35) and (2.36), respectively. We define t_0 as the time at which all the $|c_0\rangle$ atoms are scattered into the side modes, and thus it is determined from $\sinh^2(\chi_1 t_0) = N/2$.

In this later dynamical stage, see Appendix 2.9.2, the entanglement witness parameter in between the end-fire modes (e) is evaluated to be ($\lambda \equiv \lambda_{\text{ee}}$)

$$\lambda(t) = 4\sinh^2(\chi_1 t_0) - 2|\cos(\bar{\theta})\sin(2\chi_2\Delta t)|\sinh(2\chi_1 t_0), \tag{2.42}$$

where $\bar{\theta} = \theta_1 + \theta_2$. When $|\cos(\bar{\theta})| \simeq 1$, λ evolves from $2N$ down to the minimum possible negative value of $\lambda_{\text{low}} = -2$, at $\Delta t = \pi/4\chi_2$. An analogous calculation for entanglement between the end-fire mode (e) and side mode (s) gives

$$\lambda_{\text{se}}(t) = 4\sinh^2(\chi_1 t_0) - 2|\sin(\theta_2)\cos(2\chi_2\Delta t)|\sinh(2\chi_1 t_0), \tag{2.43}$$

which starts at $\lambda_{\text{se}}(t_0) = -2$ and increases to values of order $\sim N$, for proper choices of θ_2. Many of these features revealed from simple analytic models find their parallels in numerical solutions as displayed in Fig. 2.10.

The results from the two model Hamiltonians are found to depend on the initial phase difference between θ_1 and θ_2, but not the individual phases. Such a phase dependence of the results is analogous to the cases of parametric down conversion and the two-mode squeezing [7]. The phases introduced in the second stage reflects the accumulating temporal phase difference of the operators through the time evolution. In the numerical calculation it is sufficient to assign initial phases for the pump laser and the condensate or just their difference.

Without any detailed analysis, simply consider the behaviors of Eqs. (2.38) and (2.42) instead, one can already appreciate the built-in entanglement swap mechanism within the superradiant BEC in action. The entanglement created between the side mode and end-fire mode Eq. (2.38) in the initial stage, is swapped to entanglement between the two end-fire modes Eq. (2.42), due to the 2^{nd} order SR. The model Hamiltonian $\hat{H}_1$ couples the $|a_\pm\rangle \leftrightarrow |c_\mp\rangle$ modes, but leaves $|a_+\rangle \leftrightarrow |a_-\rangle$ modes decoupled at the initial times. The model Hamiltonian $\hat{H}_2$, at later times, couples the $|a_\pm\rangle \leftrightarrow |c_\pm\rangle$ states. Two noninteracting modes $|a_+\rangle \leftrightarrow |a_-\rangle$ are coupled through their common interaction with the same side mode, and become entangled due to the swap mechanism.

2.6 Numerical Calculation of the Entanglement Parameter

We study the dynamics of the entanglement parameter $\lambda(t)$ and the accompanying populations for the fields $(I_0(t),I_\pm(t))$ and the atomic states $(n_0,n_\pm(t),n_2)$. Their complete temporal evolution is governed by the Hamiltonian Eq. (2.24). Our calculation will be numerically obtained, aided by a decorrelation approximation that neglects higher order correlations. The numerical results will be illustrated and discussed in the next section.

The entanglement parameter λ, given in Eq. (2.33), is determined by the expectation values of both $\hat{a}_\pm$ operators and their products. Their equations of motion in operator forms can be derived from the full Hamiltonian Eq. (2.24).

The dynamics of two operator products is found to depend on four operator products; and four operator products depend on six operator products, and so on so forth. Such a hierarchy of operator equations is impossible to manage in general. We therefore resort to a decorrelation approximation that truncates it to a closed form. The usual treatment of this kind [59] for the SR system closes the chain early by a simple decorrelation of atomic and optical operators, which is clearly inappropriate when entanglement swap is to be studied.

We adopt a decorrelation rule that factorizes condensate and the second order side mode operators in operator products. Since quantum correlations between the condensate and other modes are expected to be weak due to the almost classical, coherent-state-like nature for the condensate and its diminishing population when the second order side mode is significantly populated at later stages of dynamics. Operators for the pump photons will also be factorized, again relying on the almost classical, coherent state nature of the pump field.

Our approach makes it possible to keep quantum correlations between the end-fire modes and the intermediate side modes. The hierarchy of equations is closed under $\langle xyz\rangle \approx \langle xy\rangle\langle z\rangle$, with $x, y \in \{1, c_\pm, c_\pm^\dagger, a_\pm, a_\pm^\dagger\}$ and $z \in \{c_0, c_0^\dagger, c_2, c_2^\dagger\}$. The resulting equations, governing the dynamics of the expectations, are given in the Appendix. These equations are solved numerically.

For the initial conditions, both the end-fire modes and side modes are taken to be their vacuum Fock states while the laser and the condensate are in coherent states. We consider a system with typical parameters of a condensate with number of atoms $N = 8 \times 10^6$ and a pump with $M = 2 \times 10^8$ photons. Additionally, phenomenological decoherence rates are introduced by assuming the same damping rates [86] for the atomic and photonic modes. The decay rates are obtained from the effective decay of the experimentally measured contrast for the atomic density distribution pattern [20]. In addition, we also explored an interesting scheme where the coupled equations (2.68-2.85) were solved, in the presence of phenomenological damping, for an initial two-mode squeezed vacuum (for the end-fire modes) with a squeezing parameter $\xi = r \exp(i\theta_r)$.

2.7 Results and Discussion

In Sec. 2.5 we discussed the origins of the entanglement swap in sequential SR. In this section, in order to provide for a more detailed and quantitative understanding, we present results obtained from numerical calculations. We will discuss the time evolution of the entanglement parameter $\lambda(t)$, between the two end-fire modes, within the parameter regime of the experiment [20]. At first, we will disregard decoherence and examine the nature of fully coherent sequential dynamics. We will show that λ attains negative values, confirming the presence of entanglement due to the swap mechanism as we intuitively discussed in the previous section. We then introduce effective damping rates specific to the experimental situation. Finally, we will examine the effect of initializing the quantum dynamics of our model system from in a two-mode (end-fire modes) squeezed vacuum, in the presence of decoherence and dissipations. We will end with investigations of the dependence of correlations on the number of condensate atoms.

2.7.1 Dynamics of Entanglement

In Fig. 2.9, we plot the temporal evolution of optical field intensities and atomic side mode populations. The plot is found to be totally symmetric with respect to $t = t_c = 0.35$ ms. The peak in the intensity after t_c is the analog of the Chiao ringing [72]. In the experiments such a complete ringing cannot be observed due to the finite lifetime of the excited levels, which is treated in the following section.

In Fig. 2.10, we plot the temporal evolution of entanglement parameters $\lambda_{\rm ee}$ (photon-photon) and $\lambda_{\rm se}$ (atom-photon) over the population dynamics, depicted in Fig. 2.9. The lower panel of Fig. 2.10 demonstrates the swap dynamics. The initial atom-photon entanglement ($\lambda_{\rm se}$) is seen to evolve continuously into entanglement between the two end-fire modes (λ). Both the parameters $\lambda_{\rm se}$ and λ is found to be able to reach down to the lowest possible value, $\lambda_{\rm low} = -2$, set by the Heisenberg uncertainty principle (as in Sec. 2.4). The complete numerical results match well with the analytic solutions, discussed previously in Sec. 2.5,

for the model Hamiltonians (2.34) at early times and (2.39) at later times.

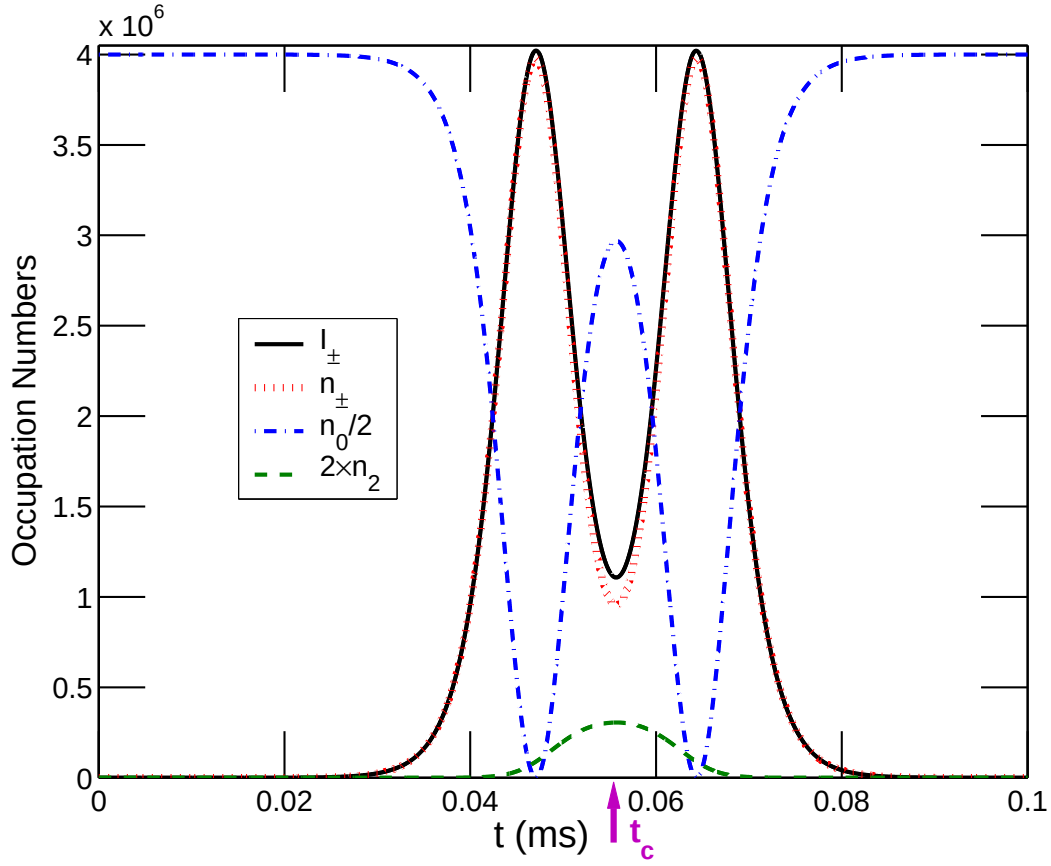

Figure 2.9: (Color online) The temporal evolutions for atomic side mode populations and optical field intensities. $I_{\pm}$, $n_{\pm}$, n_0, and n_2 denote occupancy numbers of bosonic modes $|a_{\pm}\rangle$, $|c_{\pm}\rangle$, $|c_0\rangle$, and $|c_2\rangle$, respectively. $n_{\pm}(t)$ and $I_{\pm}(t)$ overlap except for a short time interval near $t = t_c = 0.055$ms. Notice that n_0 and n_2 are scaled for visual clarity.

In the time interval of $t = 0$-0.30 ms, we find the system is dominated by the 1^{st} sequence of SR. The atomic condensate, initially in the zero-momentum state $|c_0\rangle$, is pumped into the 1^{st} order side modes $|c_{\pm}\rangle$. This is the reason for the overlap of $n_{\pm}(t)$ with $I_{\pm}(t)$ during this interval. Due to the interaction between the side modes and the end-fire modes, scattered into opposite directions, λ_{se} becomes negative in this region.

When the $|c_{\pm}\rangle$ side modes become maximally occupied at about $t = 0.30$ ms,

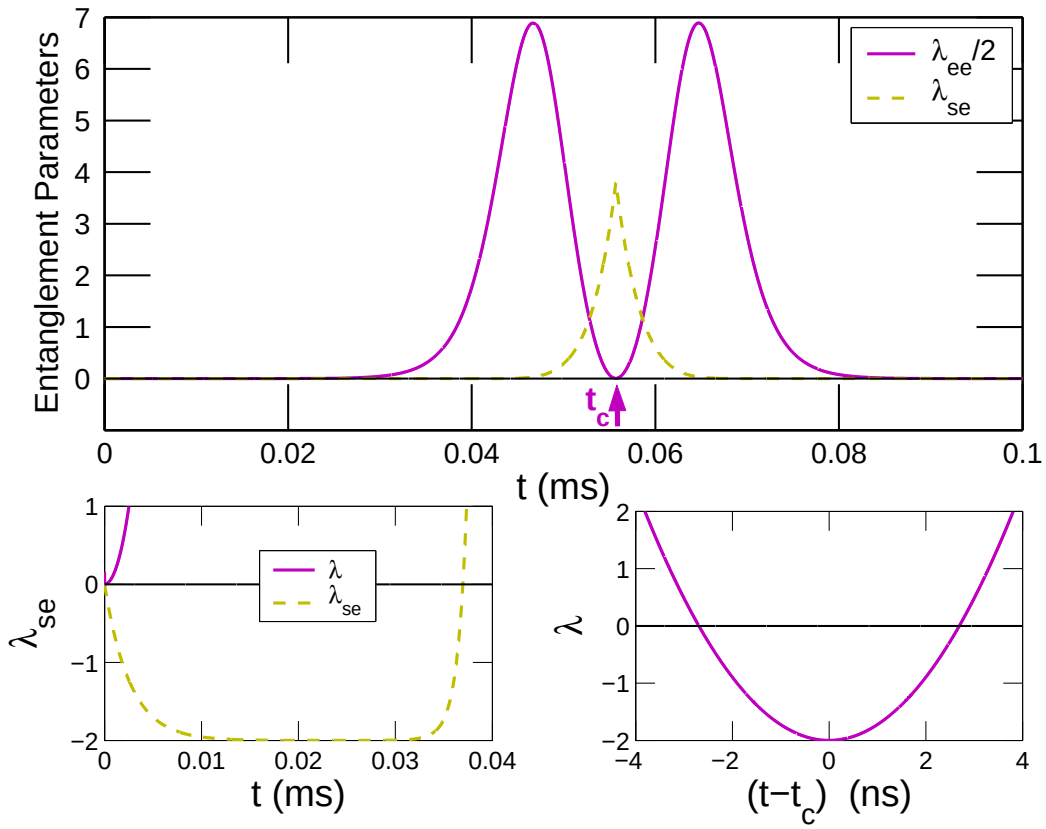

Figure 2.10: (Color online) (a) The temporal evolutions of atom-photon ($|a_{\pm}\rangle \leftrightarrow |c_{\mp}\rangle$) and photon-photon ($|a_{+}\rangle \leftrightarrow |a_{-}\rangle$) mode correlations as evidenced by the entanglement parameters $\lambda_{\rm se}$ and $\lambda \equiv \lambda_{\rm ee}$, respectively. Accompanying population dynamics is plotted in Fig. 2.9. (b) An expanded view of the early time dynamics for $\lambda_{\rm se}$ and λ; (c) an expanded view of λ around $t_c = 0.055$ ms.

the 1st sequence of SR is completed. At this time, these side modes are sufficiently populated to give rise to the 2nd sequence of SR. In the interval $t = 0.30$-0.35 ms atoms in the side modes $|c_{\pm}\rangle$ are pumped into the 2nd order side mode $|c_2\rangle$. The majority of the populations, however, oscillates back to the $|c_0\rangle$ mode because of the more dominant Rabi oscillation between the $|c_0\rangle$ and $|c_{\pm}\rangle$ modes. Two other reasons also contribute to the repopulation of the condensate mode: first, the neglect of the propagational induced departure of the end-fire mode photons from the atomic medium; and second, the neglect of the other two 2nd order side modes

$|c_{2\mathbf{k_0}\pm 2\mathbf{k_e}}\rangle$ for atoms to get into. Two end-fire modes get indirectly coupled by the entanglement swapping and between $t = 0.30$-0.35 ms $\lambda(t)$ gradually becomes negative.

Entanglement of the end-fire modes arises at $t = t_c = 0.35$ ms, when the $|c_2\rangle$ mode is maximally occupied as shown in Fig. 2.10. The minimum value of λ, which occurs at $t = t_c$, is found to coincide with the maximum value of $n_2(t)$.

When $t > t_c$, however, due to our limited mode approximation of not including even higher side modes, we cannot study any effects which could potentially give rise to higher order correlations, such as the onset of the 3$^{\text{rd}}$ sequence of SR. The oscillatory Chiao type ringing revivals in the present result after $t > t_c$ mainly arise from the exclusion of decoherence, dephasing, dissipations, and the higher order side modes in the model system. In the present work, we limited ourselves to a particular side mode pattern as actually observed in available experiments [20]. Despite its simplicity, we find our model can reasonably explain effects of decoherence and dephasing on the entanglement dynamics, which is further illustrated in the next subsection.

2.7.2 Vacuum squeezing and Decoherence

The introduction of experimentally reported decoherence rate of $\gamma/2\pi = 1.3 \times 10^4$ Hz phenomenologically into the dynamical equations for the coupled system is found to not change the nature of the entanglement and swap dynamics significantly, which is supported by the numerical results shown in Fig. 2.11. We find that λ can still become negative in certain time window, although it now falls short of reaching the theoretical lower bound of -2.

In the lower panel in Fig. 2.11 the temporal window for the negative values of λ, or the presence of entanglement is found to become narrower and the minimum value of λ, $\lambda_{\min}$, is now somewhat larger for stronger decoherence, as may be expected. According to Sec. 2.4, a less negative value of λ does not necessarily imply less entanglement, because λ is simply an entanglement witness parameter but not an entanglement measure. On the other hand, it is still beneficial to

aim for lower values of λ, because the numerical results we obtain associate lower values with longer entanglement durations, and furthermore more tolerant to decoherence, which means photon-photon entanglement can withstand the higher decoherence rates.

For this aim, we choose to consider end-fire modes which are initially in two-mode squeezed vacuum states. The lower panel in Fig. 2.11 shows that an initially two-mode squeezed vacuum, for the end-fire modes, can indeed compensate to a certain degree for decoherence. This shows that, initially induced two-mode squeezing (or entanglement) in between the end-fire modes enhances their subsequent entanglement after the entanglement swap.

This observation can be interpreted as follows based on the numerical results. Any initial correlation between the end-fire modes is lost in the early dynamical stage where the end-fire modes are entangled with the first side modes. The presence of initial correlation, however, causes the resultant atom-photon entanglement to be more resistant to decoherence. As a result, photon-photon correlations established by swapping from the atom-photon correlations in the subsequent dynamical stage also become more resistant to decoherence.

Finally, we examine the influence on λ from the number of atoms in a condensate. We find that, as illustrated in Fig. 2.12, $\lambda_{\min}$ becomes more negative for larger condensates. In the small condensate limit, $\lambda_{\min}$ is found to decrease linearly with N when the Fock vacuum is considered as initial conditions for other modes. The lower limit of -2 is never attained. When a small amount of initial squeezing is introduced, however, λ can be brought down to theoretical minimum of -2. It approaches -2 in the large condensate limit with or without any help from initial squeezing in the two end-fire modes.

In addition to the amplitude of squeezing parameter, its phase could also influence $\lambda_{\min}$. In Fig. 2.13, we plot the minimum value of the entanglement parameter as a function of the phase and amplitude of the squeezing parameter $\xi = re^{i\theta_r}$. We performed this study for a small condensate with $N = 100$ atoms and ignored the phenomenological decoherence. We find that the most efficient enhancement occurs along the line $\theta_r = \pi$. For larger condensates we find that

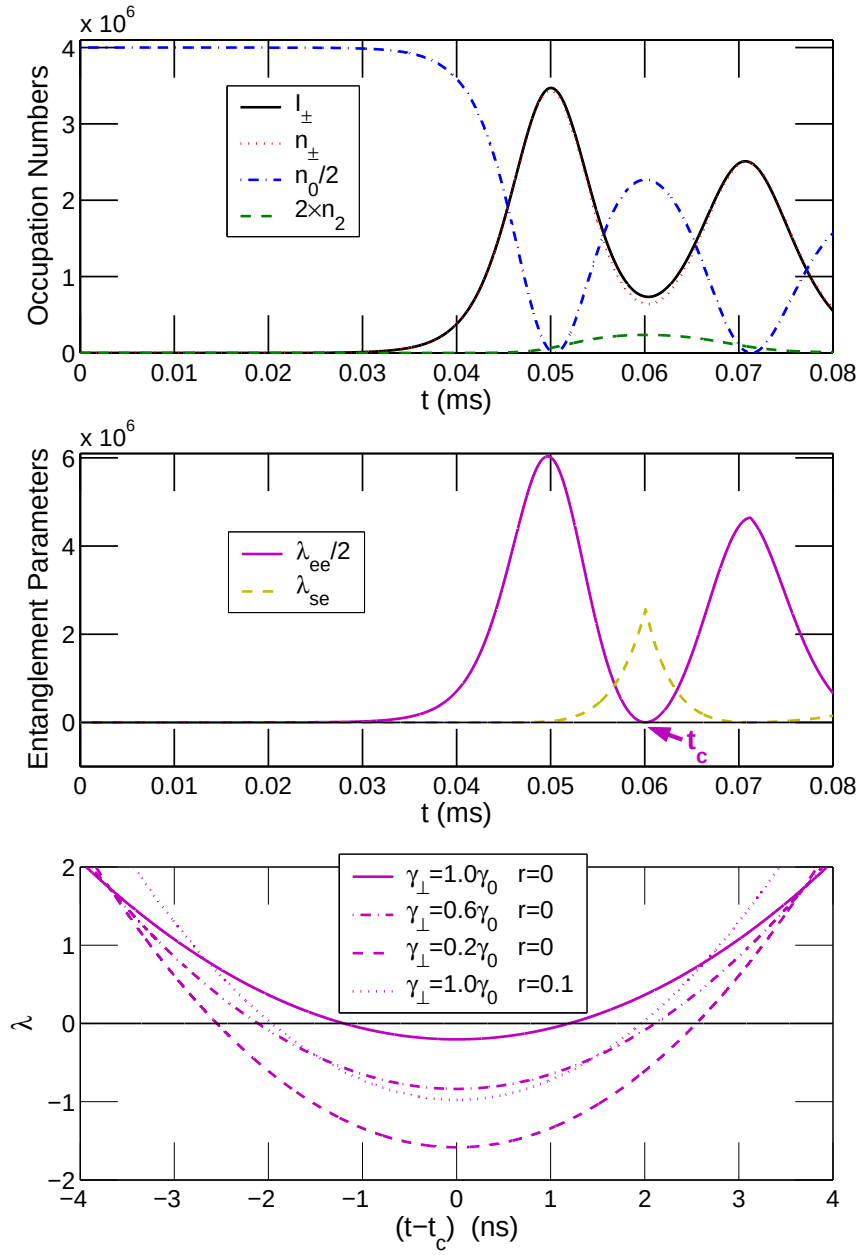

Figure 2.11: (Color online) (a) The temporal evolution of atomic and field mode populations, and (b) of entanglement parameters. A decoherence rate of $\gamma_0/2\pi = 1.3 \times 10^4$Hz is introduced without any initial squeezing. (c) An expanded view of the dependence of λ on decoherence rate γ and squeezing parameter r around $t_c = 0.060$ ms.

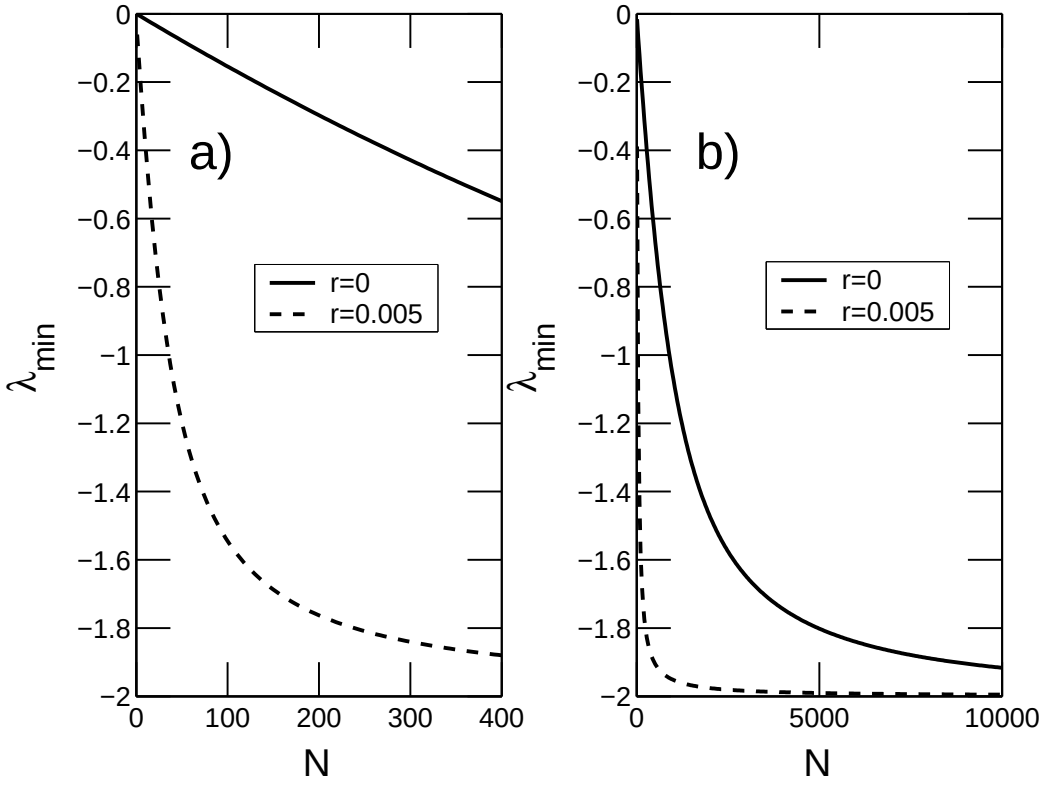

Figure 2.12: The dependence of $\lambda_{\min}$ on N in different scales. Solid lines are for an initial coherent vacuum ($r = 0$) and dashed lines are for a squeezed vacuum ($r = 0.005$ and $\theta = \pi$).

the center of Fig. 2.13, where $\lambda > 0$, spreads out to the $\theta_r = 0$ and $\theta_r = \pi$ edges, as N is increased. Entanglement is enhanced mainly along $\theta_r = 0$ and $\theta_r = \pi$ lines.

2.8 Conclusions

We investigate photon-photon entanglement between the counter-propagating end-fire modes, of a sequentially superradiant atomic Bose-Einstein condensate. We calculate the temporal evolution of the continuous variable entanglement witness parameter for suitable realistic experimental parameters in the cw-pump laser regime [20], and find that EPR like correlations can be generated between

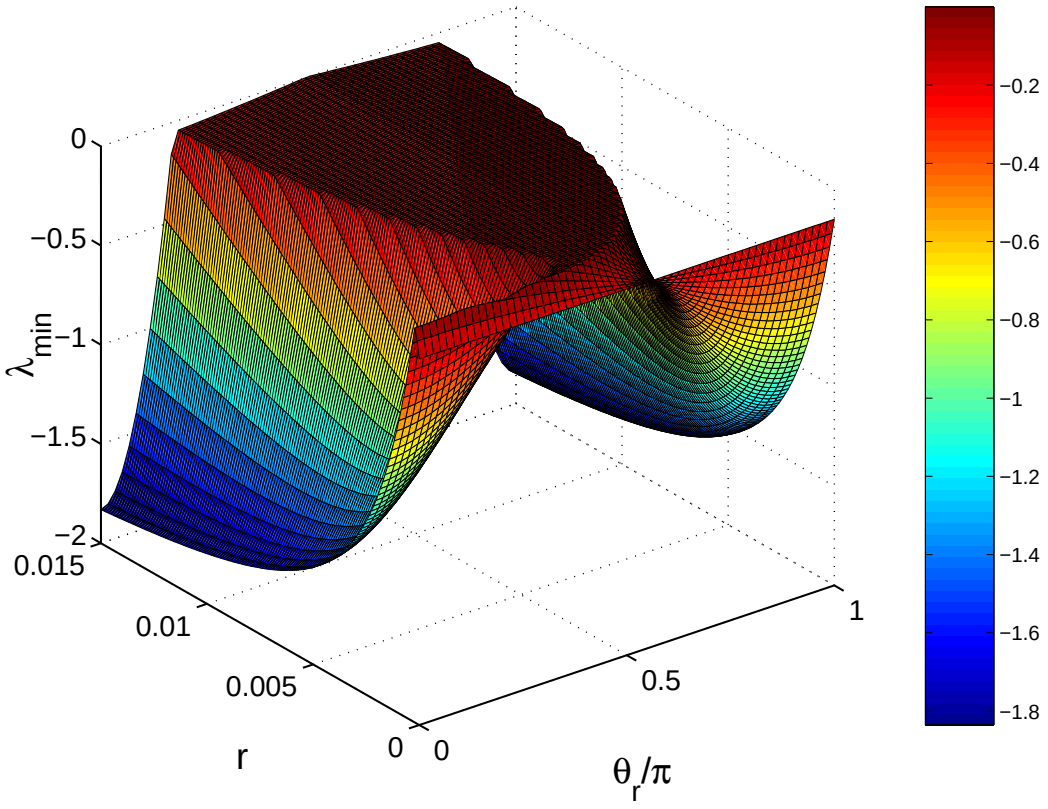

Figure 2.13: (Color online) The dependence of $\lambda_{\min}$ on r and θ_r for $N = 100$. $\lambda_{\min}$ shows a mirror symmetry for $\theta_r > \pi$.

the oppositely directed end-fire modes, despite the fact that they do not directly interact.

The generation of entanglement is shown to be due to a built-in entanglement swap mechanism we uncover in the sequential SR system. It is shown that end-fire mode photons become entangled immediately after the second sequence of the superradiance. In the second sequence, one of the end-fire modes interacts with the side mode, with which the other end-fire mode has already interacted before in the first sequence. This mechanism allows for swapping the entanglement established between the end-fire modes and the side modes in the first sequence, to the entanglement of the end-fire modes per se.

Increasing the number of atoms in the condensate, or initializing superradiance with a two-mode squeezed vacuum (for the end-fire modes), are found to be beneficial to the efficient construction of entanglement between end-fire modes, via the increasing of entanglement durations and making the entanglement more tolerant to decoherence.

The initial phase difference of the incoming pump laser and the condensate, the phase and the amplitude of the squeezing parameter for the end-fire mode vacuum, the number of atoms in a condensate and its geometric shape, all play certain roles in order to achieve the optimum ERP-like correlations in between the end-fire modes and these parameters are discussed in detail in the present manuscript for the cases of both small and large condensates.

2.9 Appendix

2.9.1 Early Times

Hamiltonian 2.34 can be decomposed into the sum of two decoupled Hamiltonians $\hat{H}_{1+} + \hat{H}_{1-}$, where

$$\hat{H}_{1\pm} = -\hbar\chi_1 \left(e^{-i\theta_1} \hat{a}_{\pm} \hat{c}_{\mp} + e^{i\theta_1} \hat{a}_{\mp}^{\dagger} \hat{c}_{\pm}^{\dagger} \right). \tag{2.44}$$

Adopting transformations

$$\hat{b}_{1\pm} = \frac{e^{-i\theta_1}/2}{\sqrt{2}} (\hat{a}_{\pm} + \hat{c}_{\mp}) \quad \text{and} \quad \hat{b}_{2\pm} = \frac{e^{-i\theta_1}/2}{\sqrt{2}} (\hat{a}_{\pm} - \hat{c}_{\mp}), \tag{2.45}$$

both of $\hat{H}_{1\pm}$ can be expressed as

$$\hat{H}_{1\pm} = -\frac{\hbar\chi_1}{2} \left[\left(\hat{b}_{1\pm}^2 + \hat{b}_{1\pm}^{2\dagger} \right) - \left(\hat{b}_{2\pm}^2 + \hat{b}_{2\pm}^{2\dagger} \right) \right], \tag{2.46}$$

wherein the motions of $\hat{b}_{1\pm}$ and $\hat{b}_{2\pm}$ are also decoupled. $\mathcal{H} = -\alpha(\hat{b}^2 + \hat{b}^{2\dagger})$ is the Hamiltonian [73] for the squeezing (single-mode), and time evolution of the operators are determined by $\hat{b}(t) = \cosh(2\alpha t)\hat{b} + i\sinh(2\alpha t)\hat{a}^{\dagger}$. Thus, time evolution of decoupled operators (2.45) becomes

$$\hat{b}_{1\pm}(t) = \cosh(\chi_1 t)\hat{b}_{1\pm}(0) + i\sinh(\chi_1 t)\hat{b}_{1\pm}^{\dagger}(0) \quad , \tag{2.47}$$

$$\hat{b}_{2\pm}(t) = \cosh(\chi_1 t)\hat{b}_{2\pm}(0) - i\sinh(\chi_1 t)\hat{b}_{2\pm}^{\dagger}(0) \quad . \tag{2.48}$$

Performing the inverse of the transformations (2.45), the time evolutions of the end-fire and side modes become

$$\hat{a}_{\pm}(t) = \cosh(\chi_1 t)\hat{a}_{\pm}(0) + ie^{i\theta_1}\sinh(\chi_1 t)\hat{c}^{\dagger}_{1\mp}(0) \quad , \tag{2.49}$$

$$\hat{c}_{\pm}(t) = \cosh(\chi_1 t)\hat{c}_{\pm}(0) + ie^{i\theta_1}\sinh(\chi_1 t)\hat{a}^{\dagger}_{2\mp}(0) \quad . \tag{2.50}$$

Entanglement and Intensity

We consider Fock-space vacuum $|a_+, a_-, c_+, c_-\rangle = |0,0,0,0\rangle$ as initial. Intensities for both end-fire and side modes display the $\sinh^2(x)$ behavior

$$\langle \hat{I}_{\pm}(t)\rangle = \langle 0,0,0,0|\hat{a}_{\pm}(t)^{\dagger}\hat{a}_{\pm}(t)|0,0,0,0\rangle = \sinh(\chi_1 t)\langle \hat{c}_{\mp}\hat{c}^{\dagger}_{\mp}\rangle = \sinh(\chi_1 t), \tag{2.51}$$

$$\langle \hat{n}_{\pm}(t)\rangle = \langle 0,0,0,0|\hat{c}_{\pm}(t)^{\dagger}\hat{c}_{\pm}(t)|0,0,0,0\rangle = \sinh(\chi_1 t)\langle \hat{a}_{\mp}\hat{a}^{\dagger}_{\mp}\rangle = \sinh(\chi_1 t), \tag{2.52}$$

that parallels the usual results [7].

Since $\langle 0|\hat{a}_{\pm}|0\rangle = \langle 0|\hat{c}_{\pm}|0\rangle = 0$ and $c^2 = \sqrt{n_{\pm}(t)/I_{\mp}(t)} = 1$, entanglement parameter in between the side and end-fire modes (2.33) simplifies to

$$\lambda_{\rm se}(t) = 2\left(\langle \hat{I}_{\pm}(t)\rangle + \langle \hat{n}_{\mp}(t)\rangle + \mathrm{sgn}(c)\langle \hat{a}^{\dagger}_{\pm}(t)\hat{c}^{\dagger}_{\mp}(t) + \hat{a}_{\pm}(t)\hat{c}_{\mp}(t)\rangle\right) \tag{2.53}$$

which reduces to

$$\lambda_{\rm se}(t) = 2\sinh^2(\chi_1 t) + \mathrm{sgn}(c)\sin\theta\sinh(2\chi_1 t). \tag{2.54}$$

Since we try to obtain the minimum value of λ, we choose $\mathrm{sgn}(c)$ oppposite to $\mathrm{sgn}(\sin\theta)$. Thus, parameter of the entanglement in between the side and end-fire modes finally becomes

$$\lambda_{\rm se}(t) = 2\sinh^2(\chi_1 t) - |\sin\theta|\sinh(2\chi_1 t). \tag{2.55}$$

The two initial in Fig. 2.8 are (2.51) and (2.55). $\lambda_{se}(t)$ continuously approaches the lower bound $\lambda_{\rm low} = -2$.

At first glance one may anticipate the strong phase ($\theta_1 = \theta_0 + \phi_1$) dependence of the ceorrelation parameter. It becomes more meaningful in the following way. Transformations $\hat{a}_0 \to \alpha_0$ and $\hat{c}_0 \to \beta_0$ set Hamiltonian (2.24) the constraint;

both $|a_0\rangle$ and $|c_0\rangle$ always in the coherent state $|\alpha_0\rangle$ and β_0. Representations of coherent state [73] in the associated continuous basis $\hat{x} = (\hat{a} + \hat{a}^\dagger)/\sqrt{2}$, which corresponds to the electric field for $\hat{a}_0$ and atomic field strength for $\hat{c}_0$, strongly depends on the phase of the coherent state α_0,β_0. Phase of α_0,β_0 creates cosine oscillations in the displaced Gaussian.

Entanglement in between the two end-fire modes can be calculated similarly. Since $c^2 = \sqrt{I_+(t)/I_-(t)} = 1$ also in this case, the parameter (2.33) takes the form

$$\lambda(t) = 2\left(\langle \hat{I}_+(t)\rangle + \langle \hat{I}_-(t)\rangle + \mathrm{sgn}(c)\langle \hat{a}_+^\dagger(t)\hat{a}_-^\dagger(t) + \hat{a}_+(t)\hat{a}_-(t)\rangle\right). \tag{2.56}$$

This returns to be

$$\lambda(t) = 4\sinh^2(\chi_1 t), \tag{2.57}$$

which is always positive $\lambda(t) > 0$ and increases with time.

Squeezed States

The two-mode squeezed states are generated by coupling a strong laser field to a crystal exhibiting strong Kerr-nonlinearity [7, 73]. Performing the parametric pump approximation for the laser field, Hamiltonian $\mathcal{H} = -\hbar\chi\left(\hat{a}_0\hat{a}_1^\dagger\hat{a}_2^\dagger + \hat{a}_0^\dagger\hat{a}_1\hat{a}_2\right)$ transforms to

$$\mathcal{H} = -\hbar\chi\left(\alpha_0^*\hat{a}_1\hat{a}_2 + \alpha_0\hat{a}_1^\dagger\hat{a}_2^\dagger\right), \tag{2.58}$$

where $\hat{a}_{1,2}$ are two different photon modes whose frequency sum up to the laser frequency $\nu_1 + \nu_2 = \nu_0$. Hamiltonian (2.58) generates the time evolution Kernel $\hat{S} = e^{\xi^*\hat{a}_1\hat{a}_2 - \xi\hat{a}_1^\dagger\hat{a}_2^\dagger}$, that is the operator generating two-mode squeezed states.

We note that (2.58) is identical with one of $\hat{H}_{1\pm}$ defined in (2.44), if we make the substitutions $\hat{a}_\pm \to \hat{a}_1$ and $\hat{c}_\mp \to \hat{a}_2$. Following similar derivations through (2.44-2.55) we finally obtain the entanglement parameter

$$\lambda(r) = 2\left(2\sinh^2(r) - |\cos\theta_r|\sinh(2r)\right), \tag{2.59}$$

where r and θ_r are the magnitude and phase of the squeezing parameter $\xi = re^{i\theta_r}$. As squeezing is increased the electric/magnetic fields of the two modes become more correlated [30].

2.9.2 Later Times

Hamiltonian $\hat{H}_2$ in (2.39) can be decomposed as $\hat{H}_2 = \hat{H}_{2+} + \hat{H}_{2-}$, where

$$\hat{H}_{2\pm} = -\hbar\chi_2 \left(e^{i\theta_2} \hat{a}_\pm^\dagger \hat{c}_\pm + e^{-i\theta_2} \hat{a}_\pm \hat{c}_\pm^\dagger \right). \tag{2.60}$$

Linear transformations

$$\hat{b}_{1\pm} = \frac{1}{\sqrt{2}}(e^{-i\theta_2/2}\hat{a}_\pm + e^{i\theta_2/2}\hat{c}_\mp) \quad \text{and} \quad \hat{b}_{2\pm} = \frac{1}{\sqrt{2}}(e^{-i\theta_2/2}\hat{a}_\pm - e^{i\theta_2/2}\hat{c}_\mp), \tag{2.61}$$

decouples (2.60) in the diagonal form

$$\hat{H}_{2\pm} = -\hbar\chi_2 \left(\hat{b}_{1\pm}^\dagger \hat{b}_{1\pm} - \hat{b}_{2\pm}^\dagger \hat{b}_{2\pm} \right), \tag{2.62}$$

that leads to time evolutions $\hat{b}_{1\pm}(t) = \hat{b}_{1\pm}(t_0)e^{i\chi_2\Delta t}$ and $\hat{b}_{2\pm}(t) = \hat{b}_{2\pm}(t_0)e^{-i\chi_2\Delta t}$. $\Delta t = t - t_0$ is the evolution time under the act of the Hamiltonian $\hat{H}_2$. we perform the back transformations from (2.59) and substitute the time evolved values $\hat{a}_\pm(t_0)$,$\hat{c}_\pm(t_0)$ (of time t_0 under $\hat{H}_1$) from (2.49,2.50) into (2.40,2.41). Thus we obtain the operators

$$\hat{a}_\pm(t) = \mathrm{C}_1\mathrm{C}_2\hat{a}_\pm + ie^{i\theta_1}\mathrm{S}_1\mathrm{C}_2\hat{c}_\mp^\dagger + ie^{i\theta_2}\mathrm{C}_1\mathrm{S}_2\hat{c}_\pm - e^{i(\theta_1+\theta_2)}\mathrm{S}_1\mathrm{S}_2\hat{a}_\mp^\dagger, \tag{2.63}$$

$$\hat{c}_\pm(t) = \mathrm{C}_1\mathrm{C}_2\hat{c}_\pm + ie^{i\theta_1}\mathrm{S}_1\mathrm{C}_2\hat{a}_\mp^\dagger + ie^{i\theta_2}\mathrm{C}_1\mathrm{S}_2\hat{a}_\pm - e^{i(\theta_1+\theta_2)}\mathrm{S}_1\mathrm{S}_2\hat{c}_\mp^\dagger, \tag{2.64}$$

where $\mathrm{C}_1 \equiv \cosh(\chi_1 t_0)$, $\mathrm{S}_1 \equiv \sinh(\chi_1 t_0)$ and $\mathrm{C}_2 \equiv \cos(\chi_2\Delta t)$, $\mathrm{S}_2 \equiv \sin(\chi_2\Delta t)$ shorthand notations are adopted.

The entanglement parameter in between the two end-fire modes, is calculated form (2.56) as

$$\lambda(t) = 2\left(2\sinh^2(\chi_1 t_0) + \mathrm{sgn}(c)\cos(\bar{\theta})\sinh(2\chi_1 t_0)\sin(2\chi_1\Delta t)\right), \tag{2.65}$$

where $\bar{\theta} = \theta_1 + \theta_2$. In order to obtain λ at the minimum we choose the $\mathrm{sgn}(c)$ opposite to $\mathrm{sgn}\big[\cos(\bar{\theta})\sin(2\chi_1\Delta t)\big]$. Finally, we obtain the photon-photon correlation parameter as

$$\lambda(t) = 2\left(2\sinh^2(\chi_1 t_0) - |\cos(\bar{\theta})\sin(2\chi_1\Delta t)|\sinh(2\chi_1 t_0)\right). \tag{2.66}$$

This behavior is plotted in the later times of Fig. 2.8.

The behavior of atom-photon entanglement parameter at later times is calculated similar to be

$$\lambda_{\rm se}(t) = 4\sinh^2(\chi_1 t_0) - 2|\sin(\theta_2)\cos(2\chi_2\Delta t)|\sinh(2\chi_1 t_0), \tag{2.67}$$

by inserting (2.63,2.64) into (2.56). We note that expectations in (2.56) are to be calculated in the vacuum initial $|0,0,0,0\rangle$ state, too.

2.9.3 Dynamical Equations

We calculate temporal evolution of entanglement parameter $\lambda(t)$, given in (2.33), starting from the Heisenberg operator equations, obtained from (2.24). We evaluate the expectations for both single operators and two operator products. We arrive at a closed set from the expectations via performing decorrelation approximation, in parallel with the development and understanding of the swap mechanism (Sec. 2.5).

The resulting closed set of equations for expectation values are given through Eqs. (2.68-2.85), where time is scaled by frequency $\alpha = g^2/2\Delta$ with $g \simeq 2 \times 10^3$ Hz, while operators are not scaled. α is related to γ of Ref. [86], as $\gamma = \sqrt{M}\alpha =$ 10.7 Hz. Phenomenological decay rates can be introduced in Eqs. (2.68-2.85) by scaling $\gamma_\perp = 1.3 \times 10^4$Hz with α. However, since the decay rates are introduced, in [86], for three-operator products, we use $\gamma_\perp/3$ for single operators and $2\gamma_\perp/3$ for two operator products. We have also checked the parallelism of our density dynamics with [86], which are in good agreement with the experiment [20].

$$\frac{d\langle a_{\pm}\rangle}{dt} = i\langle a_0\rangle\Big(\langle c_{\mp}^{\dagger}\rangle\langle c_0\rangle + \langle c_2^{\dagger}\rangle\langle c_{\pm}\rangle\Big), \tag{2.68}$$

$$\frac{d\langle a_0\rangle}{dt} = i\Big(\langle a_- c_+\rangle\langle c_0^{\dagger}\rangle + \langle a_- c_-^{\dagger}\rangle\langle c_2\rangle + \langle a_+ c_-\rangle\langle c_0^{\dagger}\rangle + \langle a_+ c_+^{\dagger}\rangle\langle c_2\rangle\Big), \tag{2.69}$$

$$\frac{d\langle c_{\pm}\rangle}{dt} = i\Big(\langle a_0\rangle\langle a_{\mp}^{\dagger}\rangle\langle c_0\rangle + \langle a_0\rangle^*\langle a_{\pm}\rangle\langle c_2\rangle\Big), \tag{2.70}$$

$$\frac{d\langle c_0\rangle}{dt} = i\langle a_0\rangle^*\Big(\langle a_- c_+\rangle + \langle a_+ c_-\rangle\Big), \tag{2.71}$$

$$\frac{d\langle c_2\rangle}{dt} = i\langle a_0\rangle\Big(\langle a_-^{\dagger} c_-\rangle + \langle a_+^{\dagger} c_+\rangle\Big), \tag{2.72}$$

$$\begin{aligned}\frac{d\langle a_+ a_-\rangle}{dt} &= i\langle a_0\rangle\Big(\langle a_- c_-^{\dagger}\rangle\langle c_0\rangle + \langle a_- c_+\rangle\langle c_2^{\dagger}\rangle \\ &+ \langle a_+ c_+^{\dagger}\rangle\langle c_0\rangle + \langle a_+ c_-\rangle\langle c_2^{\dagger}\rangle\Big),\end{aligned} \tag{2.73}$$

$$\begin{aligned}\frac{d\langle a_+ a_-^{\dagger}\rangle}{dt} &= i\Big(\langle a_0\rangle\langle a_-^{\dagger} c_-^{\dagger}\rangle\langle c_0\rangle + \langle a_0\rangle\langle a_-^{\dagger} c_+\rangle\langle c_2^{\dagger}\rangle \\ &- \langle a_0\rangle^*\langle a_+ c_+\rangle\langle c_0^{\dagger}\rangle + \langle a_0\rangle^*\langle a_+ c_-^{\dagger}\rangle\langle c_2\rangle\Big),\end{aligned} \tag{2.74}$$

$$\frac{d\langle a_{\pm}^2\rangle}{dt} = 2i\langle a_0\rangle\Big(\langle a_{\pm} c_{\mp}^{\dagger}\rangle\langle c_0\rangle + \langle a_{\pm} c_{\pm}\rangle\langle c_2^{\dagger}\rangle\Big), \tag{2.75}$$

$$\begin{aligned}\frac{d\langle c_+ c_-\rangle}{dt} &= i\Big(\langle a_0\rangle\langle a_-^{\dagger} c_-\rangle\langle c_0\rangle + \langle a_0\rangle^*\langle a_+ c_-\rangle\langle c_2\rangle \\ &+ \langle a_0\rangle\langle a_+^{\dagger} c_+\rangle\langle c_0\rangle + \langle a_0\rangle^*\langle a_- c_+\rangle\langle c_2\rangle\Big),\end{aligned} \tag{2.76}$$

$$\begin{aligned}\frac{d\langle c_+ c_-^{\dagger}\rangle}{dt} &= i\Big(\langle a_0\rangle\langle a_-^{\dagger} c_-^{\dagger}\rangle\langle c_0\rangle + \langle a_0\rangle^*\langle a_+ c_-^{\dagger}\rangle\langle c_2\rangle \\ &- \langle a_0\rangle^*\langle a_+ c_+\rangle\langle c_0^{\dagger}\rangle - \langle a_0\rangle\langle a_-^{\dagger} c_+\rangle\langle c_2^{\dagger}\rangle\Big),\end{aligned} \tag{2.77}$$

$$\frac{d\langle c_{\pm}^2\rangle}{dt} = 2i\Big(\langle a_0\rangle\langle a_{\mp}^{\dagger} c_{\pm}\rangle\langle c_0\rangle + \langle a_0\rangle^*\langle a_{\pm} c_{\pm}\rangle\langle c_2\rangle\Big), \tag{2.78}$$

$$\begin{aligned}\frac{d\langle a_{\pm} c_{\mp}\rangle}{dt} &= i\Big(\langle a_0\rangle\langle c_{\mp}^{\dagger} c_{\mp}\rangle\langle c_0\rangle + \langle a_0\rangle\langle c_{\pm} c_{\mp}\rangle\langle c_2^{\dagger}\rangle \\ &+ \langle a_0\rangle\langle a_{\pm} a_{\pm}^{\dagger}\rangle\langle c_0\rangle + \langle a_0\rangle^*\langle a_{\pm} a_{\mp}\rangle\langle c_2\rangle\Big),\end{aligned} \tag{2.79}$$

$$\begin{aligned}\frac{d\langle a_{\pm} c_{\pm}^{\dagger}\rangle}{dt} &= i\Big(\langle a_0\rangle\langle c_{\pm}^{\dagger} c_{\mp}^{\dagger}\rangle\langle c_0\rangle + \langle a_0\rangle\langle c_{\pm} c_{\pm}^{\dagger}\rangle\langle c_2^{\dagger}\rangle \\ &- \langle a_0\rangle^*\langle a_{\pm} a_{\mp}\rangle\langle c_0^{\dagger}\rangle - \langle a_0\rangle^*\langle a_{\pm} a_{\pm}^{\dagger}\rangle\langle c_2^{\dagger}\rangle\Big),\end{aligned} \tag{2.80}$$

$$\begin{aligned}\frac{d\langle a_{\pm} c_{\pm}\rangle}{dt} &= i\Big(\langle a_0\rangle\langle c_{\pm} c_{\mp}^{\dagger}\rangle\langle c_0\rangle + \langle a_0\rangle\langle c_{\pm}^2\rangle\langle c_2^{\dagger}\rangle \\ &+ \langle a_0\rangle\langle a_{\pm} a_{\mp}^{\dagger}\rangle\langle c_0\rangle + \langle a_0\rangle^*\langle a_{\pm}^2\rangle\langle c_2\rangle\Big),\end{aligned} \tag{2.81}$$

$$\begin{aligned}\frac{d\langle c_{\pm}^{\dagger} c_{\pm}\rangle}{dt} &= i\Big(-\langle a_0\rangle^*\langle a_{\mp} c_{\pm}\rangle\langle c_0^{\dagger}\rangle - \langle a_0\rangle\langle a_{\pm}^{\dagger} c_{\pm}\rangle\langle c_2^{\dagger}\rangle \\ &+ \langle a_0\rangle\langle a_{\mp}^{\dagger} c_{\pm}^{\dagger}\rangle\langle c_0\rangle + \langle a_0\rangle^*\langle a_{\pm} c_{\pm}^{\dagger}\rangle\langle c_2\rangle\Big),\end{aligned} \tag{2.82}$$

$$\begin{aligned}
\frac{d\langle c_0^\dagger c_0\rangle}{dt} &= i\Big(-\langle a_0\rangle\langle a_-^\dagger c_+^\dagger\rangle\langle c_0\rangle - \langle a_0\rangle\langle a_+^\dagger c_-^\dagger\rangle\langle c_0\rangle \\
&+ \langle a_0\rangle^*\langle a_- c_+\rangle\langle c_0^\dagger\rangle + \langle a_0\rangle^*\langle a_+ c_-\rangle\langle c_0^\dagger\rangle\Big), \qquad (2.83)\\
\frac{d\langle c_2^\dagger c_2\rangle}{dt} &= i\Big(-\langle a_0\rangle^*\langle a_- c_-^\dagger\rangle\langle c_2\rangle - \langle a_0\rangle^*\langle a_+ c_+^\dagger\rangle\langle c_2\rangle \\
&+ \langle a_0\rangle\langle a_-^\dagger c_-\rangle\langle c_2^\dagger\rangle + \langle a_0\rangle\langle a_+^\dagger c_+\rangle\langle c_2^\dagger\rangle\Big), \qquad (2.84)\\
\frac{d\langle a_\pm^\dagger a_\pm\rangle}{dt} &= i\Big(-\langle a_0\rangle^*\langle a_\pm c_\mp\rangle\langle c_0^\dagger\rangle - \langle a_0\rangle^*\langle a_\pm c_\pm^\dagger\rangle\langle c_2\rangle \\
&+ \langle a_0\rangle\langle a_\pm^\dagger c_\mp^\dagger\rangle\langle c_0\rangle + \langle a_0\rangle\langle a_\pm^\dagger c_\pm\rangle\langle c_2^\dagger\rangle\Big). \qquad (2.85)
\end{aligned}$$

Chapter 3

Photonic Band Gap in the Triangular Lattice of BEC vortices

3.1 Introduction

When a Bose-Einstein condensate (BEC) is rotated, after a certain critical frequency, vortices start to form. For high enough rotation frequency, these vortices become large in number and distribute in a periodical structure [75–78]. The usual structure is a triangular lattice, but other lattice types may as well occur, depending on the strength of the inter-particle interactions [80]. The density profile is periodically distributed vortices on an envelope function, which decreases toward the edge of the condensate [77, 78]. The envelope is a slowly varying function compared to the vortex periodicity, such that few hundred vortices are observable experimentally [79]. The imaging of the lattice was accomplished while the condensate is in the trap in Ref. [79], different from the usual ballistic expansion imaging [75, 76, 81–83].

This periodicity simulates 2D photonic band gap (PBG) materials. Despite the common PBG material [84], however, the lattice parameter of a BEC vortex lattice is continuously tunable via the rotation frequency. Moreover, lattice type can be changed, while the BEC is in the trap, by controlling the inter-particle interaction strength by Feshbach resonances [85].

We recently proposed [2, 86] to directly measure the rotation frequency of BEC using the reflection from a directional PBG pulse propagation, stopped only in certain directions and allowed in others. The chopping in the reflected pulse, propagating through BEC lattice, measures its rotation frequency.

The difficulty is, however, to establish the high enough index contrast between the vortex cores and the bulk of the BEC. BEC is dilute gaseous atomic medium, as such exhibits dispersion and polarization only in the high absorptive frequency regimes. Necessary contrast is achieved using one of the index-enhancement schemes [73, 87], which are based on the atomic quantum coherence. Coupling the excited (or ground) state to other auxiliary levels, it is possible to obtain high polarization response without absorption [73]. Quantum interference of various absorption paths allows the retainment of the atoms in the excited level with cancelling absorption.

Dielectric response, obtained using index enhancement schemes, is complex in structure. Gain and absorption regimes crossover the zero absorption frequency and more over they are very strong [see Fig. 3.2]. Dielectric function varies rapidly with the frequency and both real and imaginary parts of it changes sign. Checking the existence of the PBG at exactly on the zero-absorption frequency is straightforward. However, the determination of the frequency width of the band gap about such a point, surrounded by both gain and absorption, is more challenging [2].

In this Chapter, we examine the photonic band structure of a triangular vortex lattice. We investigate the frequency width of the photonic band gap, for a complex frequency-dependent dielectric function. The unusual dielectric response is due to the index enhancement scheme [87], which is utilized for high index contrast. In order to be able to determine the band gap width, we also examine the complex Poynting vector beside the complex wave vector. We first review our previous results [2, 86] based upon upper level microwave scheme for index enhancement. After that we shall consider Raman scheme and show that it is capable to generate much wider band gaps.

Although in the literature there exists abundant studies on photonic crystals (PC), the ones considering the complex frequency-dependent dielectric function are rare. There exist few studies, but these are focused on the examination of the effects of metallic components to the bands of PC [88–94]. In the widely used Drude model, absorption is of negligible importance in the transparency window. Small, but realistic, amount of absorption does not change the band structure much [90]. On the other hand in the region of appreciable absorption there may occur no gap [93].

The dielectric function, we deal here, is completely different from the ones considered up to present. BEC offers gain regimes, as well as absorption, beyond the enhancement window [87], which resembles the lasing without inversion [73]. To our knowledge, PBG of such a periodic structure, composed of index-enhanced media, is investigated in [2] for the first time. The gain regime is important for the understanding of the lasing properties of PC [95], as well as absorptive properties

are advantageous in various applications [96].

The Chapter is organized as follows. In Sec. 3.2 we describe the dielectric function $\epsilon(\vec{r},\omega)$ inside the vortex PC, that is enhanced with upper-level microwave scheme [87]. In Sec. 3.3, we deduce the matrix equations from the master equation of PC. We show how to obtain the band structure for a complex frequency-dependent dielectric susceptibility. In Sec. 3.4 A we present the resulting photonic bands for two different lattice constants. In Sec. 3.4 B we discuss the frequency width of the band gap in the presence of gain and absorption. In Sec. 3.5 we present the band results for Raman index enhancement scheme. We summarize our results in Sec. 3.6.

3.2 Dielectric function of the vortex lattice

Among the various index enhancement schemes [87], upper-level microwave scheme [see Fig. 3.1] leads to the strongest index contrast with vanishing absorption [Fig. 3.2]. Another one is the Raman scheme [87], discussed in Sec. 3.5, generates weaker enhancement, but in a broader frequency window. The former one results in a stronger stoppage at a single frequency, while the latter operates as a weaker blocker over a broader frequency range.

In the upper-level microwave scheme, the excited level a is coupled to an auxiliary level c via a strong resonant microwave field of Rabi frequency Ω_μ. The weak optical field E, coupling the ground state b to excited state a, is the test field. Its dielectric response is calculated. Alternative absorption path $b \rightarrow c \rightarrow a$ destructively interfere with the direct absorption path $b \rightarrow a$ [73]. This quantum interference, due to the phase difference, cancel the absorption of the probe pulse E at a certain frequency, plotted in Fig. 3.2. At the same time, high polarization is obtained by keeping population at the excited level a.

Upper-microwave scheme, for $r_c = \Omega_\mu = \gamma$, results in the complex dielectric

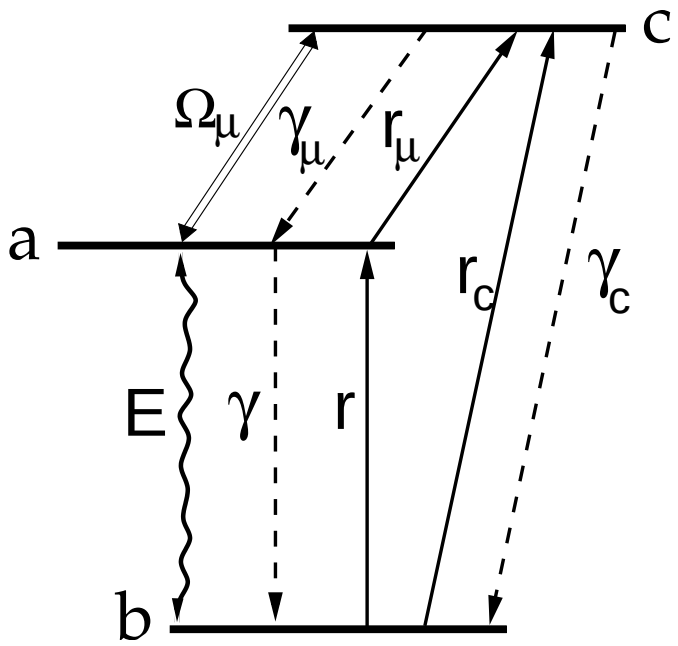

Figure 3.1: Upper-level microwave scheme for index enhancement [87]. Upper two levels a and c are coupled via a strong microwave field of Rabi frequency Ω_μ. Weak probe field E, of optical frequency ω is coupled to levels a and b. Decay (γ) and pump (r) rates are indicated.

susceptibility $\chi(\omega) = \chi'(\omega) + i\chi''(\omega)$ of real χ' and imaginary parts χ'' are [87]

$$\chi'(\varpi) = \frac{12N\lambda^3}{13\pi^2}\frac{\varpi}{9 - 3\varpi^2 + 4\varpi^4} \tag{3.1}$$

$$\chi''(\varpi) = -\frac{3N\lambda^3}{13\pi^2}\frac{-3 + 2\varpi^2}{9 - 3\varpi^2 + 4\varpi^4}\,, \tag{3.2}$$

where λ is the wavelength of the $a \rightarrow b$ transition, and N is the number density of the particles. $\varpi = (\omega - \omega_{ab})/\gamma$ is the negative detuning, scaled with the decay rate of decoherence γ.

Since (3.1) and (3.2) are valid for the interaction of the field single atom, we also perform the local field correction [97] as $\chi_{\rm loc}(\varpi) = \frac{\chi(\varpi)}{1-\chi(\varpi)/3}$. The real and imaginary parts of dielectric function $\epsilon_{\rm loc}(\varpi) = 1 + \chi_{\rm loc}(\varpi)$ are plotted in Fig. 3.2, for Rubidium-87 gas. $\Omega_0 = 2.37 \times 10^{15}$ Hz is the zero absorption frequency which corresponds to $\varpi_0 = (\Omega_0 - \omega_{ab})/\gamma \simeq 1.22$ in scaled form.

The physical levels corresponding to b,a, and c are $5s_{1/2}$, $5p_{1/2}$, and $6s_{1/2}$ fine-structure levels of Rb-87. Transition wavelengths are $\lambda = 794$ nm and $\lambda_\mu = 1.32\,\mu$m for the probe and the microwave fields, respectively. The lifetime of the excited level a ($5p_{1/2}$) is 27 ns, which gives a decay rate $\gamma = 2\pi \times 6$ MHz.

The spatial periodicity of the dielectric response is simulated with hexagonal Wigner-Seitz unit cells, each including a vortex at the center and evolve to bulk at the corners. We use the Padé's analytical form [98]

$$\rho(r) = \frac{r^2(0.3437 + 0.0286r^2)}{1 + 0.3333r^2 + 0.0286r^4}\,, \tag{3.3}$$

where r is scaled with the coherence length $\xi = 1/\sqrt{8\pi N a_{sc}}$. This density behavior is valid in one unit cell. $\rho(r)$ becomes zero at the center and approaches to 1 towards the edges of the hexagon. The the dielectric function becomes

$$\epsilon_{\rm loc}(\vec{r}, \varpi) = 1 + \rho(\vec{r})\chi_{\rm loc}(\varpi)\,. \tag{3.4}$$

inside one unit cell and repeats itself within the triangular lattice periodicity.

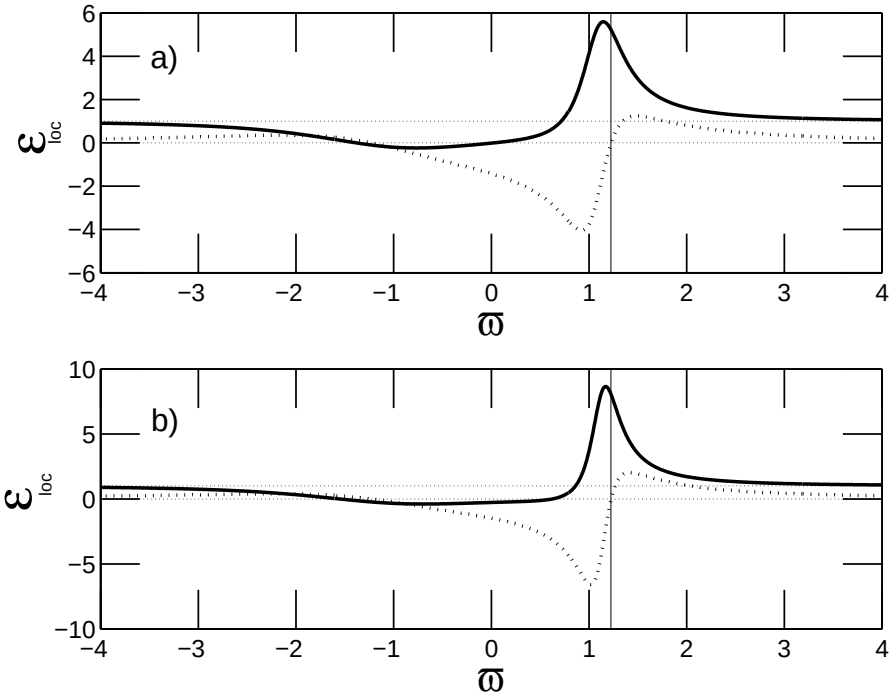

Figure 3.2: Real (solid-line) and imaginary (doted-line) parts of local dielectric function $\epsilon_{\rm loc}(\omega)$ as a function of scaled frequency $\varpi = (\omega - \omega_{ab})/\gamma$, for the particle densities (a) $N = 5.5 \times 10^{20}\,\mathrm{m}^{-3}$ and (b) $N = 6.6 \times 10^{20}\,\mathrm{m}^{-3}$. Vertical solid line indicates the scaled enhancement frequency $\varpi_0 \simeq 1.22$, where $\epsilon''_{\rm loc}(\varpi)$ vanishes. (a) $\epsilon = \epsilon_{\rm loc}(\varpi_0) = 5.2$ and (b) $\epsilon = \epsilon_{\rm loc}(\varpi_0) = 8.0$.

3.3 Calculation of the Photonic Bands

In our calculations, we assume that lattice is composed of infinite number of unit cells. In our past work [86], we have numerically validated that the positions of the band gaps are not much affected by the finite size and small imperfection of the lattice. Dielectric function $\epsilon(\vec{r}, \varpi)$, in one unit cell, is given in equation 3.4.

In 2D PC there exist two independent modes [84]. When the $\vec{H}/\vec{E}$ field is perpendicular to the plane of periodicity, the mode is called as transverse electric/magnetic, or by short hand notation TE/TM. We summarize the calculations here, but details can be found in [2].

The spatial dependence in the Master (eigenvalue) equation

$$\vec{\nabla} \times \left(\frac{1}{\epsilon(\vec{r}, \omega)} \vec{\nabla} \times \vec{H}(\vec{r}) \right) = \left(\frac{\omega}{c} \right)^2 \vec{H}(\vec{r}) \tag{3.5}$$

is decomposed into the plane waves, in accordance with the Bloch-Floquet Theorem [99]. This way a matrix equation is obtained. Using the condition of the determinant of the matrix to be zero, the relation of ω-k is solved.

There exists two possible ways to construct a relation between ω and k. In the first, we put real-ω values as input and obtain the complex-k values. In the second, we put real-k values and extract complex-ω values. The first method is useful when the spatial attenuation of the subject of interest is the spatial attenuation of the probe pulse. Second one is useful in determining the attenuation time.

The two approaches give parallel results [90], but cannot be connected (or compared) directly. We choose the real-ω/complex-k method. This is because we are curious about if the penetration depth is less or greater than a few tens of lattice cites. In other words, we ask for if the band gap is strong enough to stop the probe beam or it partially transmits it.

3.4 Results and Discussion

3.4.1 Band Structures

When the dielectric function is frequency independent, $\epsilon(\omega) = \epsilon$, master equation (3.5) is scalable with the lattice parameter a. This makes the structure of the photonic bands, when expressed in terms of the scaled frequency $\omega' = \omega a/2\pi c$, independent of the lattice dimensions. Such a scaling, however, is not possible for the frequency-dependent dielectric response. This is because, susceptibilities (3.1) and (3.2) are altered with the ratio of γ and $2\pi c/a$. This introduces a new variable, both for theoretical and experimental usage, since a is continuously tunable in rotating BEC.

We use the tunability of the lattice parameter a to obtain stronger stoppage at the enhancement frequency Ω_0 ($\varpi_0 = 1.22$ in Fig. 3.2).

We compute the photonic bands for two different dielectric functions, plotted in Fig. 3.2a and 3.2b, and present the results in Figs. 3.4 and 3.5, respectively. Fig. 3.3a and 3.3b are respective intermediate-steps for Fig. 3.4 and 3.5, to be mentioned in the following paragraph.

Our method of approach is as follows. First, we obtain the constant dielectric bands, in Fig. 3.3, at the enhancement frequency $\epsilon = \epsilon(\Omega_0)$. At that frequency dielectric constant is real and polarization is strong, see Fig. 3.2. Second, we arrange the lattice parameter such that enhancement frequency is placed at the center of the gap. That is $\Omega_0 = \omega'_g(2\pi c/a)$, which gives the optimum lattice dimension as

$$a = \omega'_g \frac{2\pi c}{\omega_{ab} + \varpi_0 \gamma} \quad . \tag{3.6}$$

Here ω'_g is the scaled center of the gap frequency, to be read from constant dielectric bands of Fig. 3.3. Third, we obtain the photonic bands of frequency-dependent dielectric $\epsilon_{\rm loc}(\vec{r}, \varpi)$ of Eq. 3.4 in Figs. 3.4 and 3.5, with this arrangement.

In Fig. 3.3, we give the constant dielectric photonic bands of vortex lattice for two different parameter sets. The first set, $N = 5.5 \times 10^{20}$ m^{-3} and $a = 10\xi$,

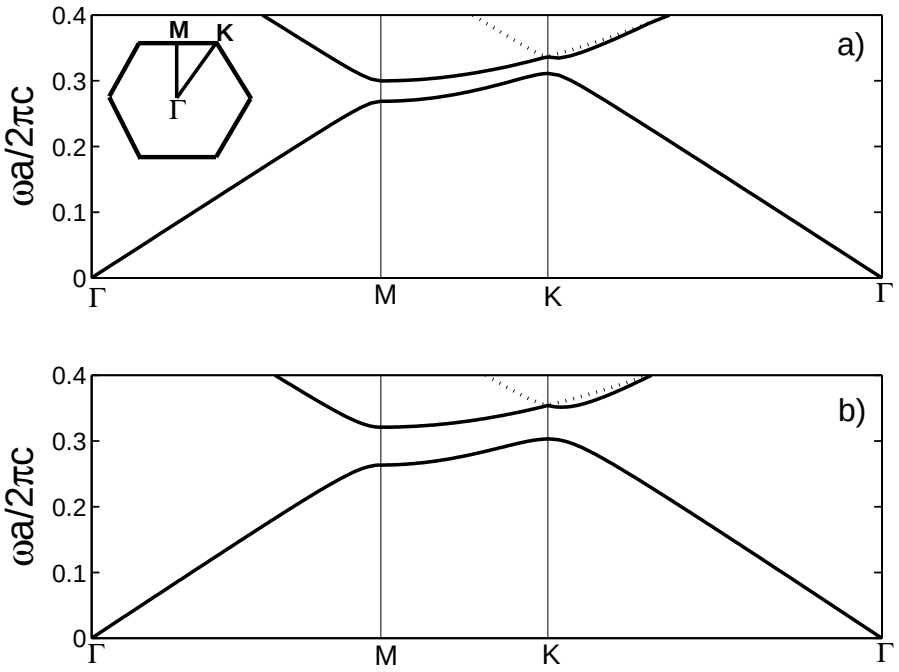

Figure 3.3: TE modes of a triangular vortex lattice with frequency independent ϵ. (Symmetry points and the irreducible Brillouin zone of a triangular lattice are indicated in the inset.) Dielectric constants and lattice parameters are (a) $\epsilon = 5.2$ and $a = 10\xi$, (b) $\epsilon = 8$ and $a = 4.5\xi$. Filling fractions of vortices, $f = (2\pi/\sqrt{3}) \times (R^2/a^2)$ with effective radius $R \simeq 2\xi$, are 15% and 71%, respectively. Dielectric constant is the value of dielectric function (3.4) at the enhancement frequency, $\epsilon = \epsilon_{\rm loc}(\varpi_0)$. Density profile of the unit cell is treated using the Padé approximation [98]. (a) There exists a directional pseudo-band gap with midgap frequency at $\omega_g' = 0.285$. (b) There is a complete band gap with gap center at $\omega_g' = 0.31$.

generates a directional pseudogap in the ΓM direction. Note that the value of dielectric constant, used in Fig. 3.3a, is the value of the dielectric function (Fig. 3.2a) at the enhancement frequency, $\epsilon = \epsilon_{\rm loc}(\varpi_0) = 5.2$. The a/ξ ratio determines the density profile in the hexagonal unit cell, according to function (3.3).

The dielectric band gap lies in the frequency range $\omega = (0.27 - 0.31)(2\pi c/a)$, with its center is at $\omega_g = 0.285(2\pi c/a)$. Then, in order to obtain the strongest stoppage at the enhancement frequency, we arrange the lattice constant to $a =$ 226 nm according to (3.6). The resultant bands for the complex frequency-dependent dielectric response, depicted in Fig. 3.2a, is given in Fig. 3.4. The imaginary part of the wave vector, k_I, is also included.

The second parameter set, $N = 6.6 \times 10^{20}$ m^{-3} and $a = 4.5\xi$, is chosen such that there occurs a complete band gap, see Fig. 3.3, at the enhanced dielectric constant $\epsilon = \epsilon_{\rm loc}(\varpi_0) = 8$ (Fig. 3.2b). The complete gap lies in the frequency range $\omega = (0.30 - 0.32)(2\pi c/a)$, with the midgap frequency $\omega_g = 0.31(2\pi c/a)$. Note that, for the choice of $a = 4.5\xi$ filling factor of the vortex is higher. Then, for this parameter set, we arrange the lattice constant to $a = 246$ nm. Photonic bands for complex frequency-dependent dielectric function, which is plotted in Fig. 3.2b, is depicted in Fig. 3.5.

In Figs. 3.4a and 3.5a we plot the frequency with respect to the real part of the wave vector, k_R, for all bands. In Figs. 3.4b and 3.5b we give the imaginary parts of the wave vector, k_I, corresponding to each band. The enhancement frequency $\varpi_0 = 1.22$ is marked in all plots.

When the dielectric function is real, it is very easy to identify the band gaps. If there is propagation, k comes out to be real. If the frequency is in the band gap, k becomes complex, with k_R is on the band edge. In the case of complex $\epsilon(\omega)$, however, identification of the frequency range of the band gap is not straightforward. At a certain frequency, where ϵ is real, there exists a band gap, if k_I is nonzero. For other frequency values, where ϵ is complex, the nonzero value of k_I may occur due to the absorption, as well as a reflector band gap. Even considering the gain regions about the enhancement frequency, ϖ_0 in Fig. 3.2, situation becomes more complicated. We discuss this in the following subsection,

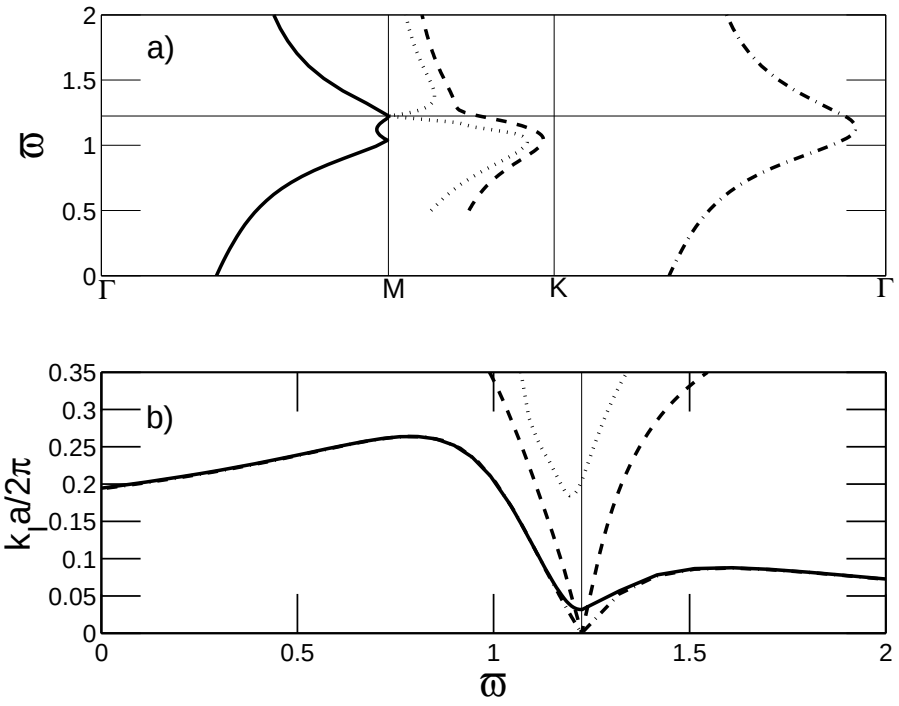

Figure 3.4: (a) TE modes of triangular vortex lattice with frequency dependent dielectric function $\epsilon_{\rm loc}(\varpi)$ (Fig. 3.2), and (b) imaginary parts of the wave vector k_I corresponding to each mode. Particle density is $N = 5.5 \times 10^{20}$ m^{-3} and lattice constant is $a = 10\xi$. Enhancement frequency Ω_0 is tuned to the band gap at the M edge ($\omega_g = 0.285(2\pi c/a)$) of the constant dielectric case (Fig. 3.3a). MK bands are plotted in a limited region, because of high k_I values out of the given frequency region. There exists a directional gap in the ΓM propagation direction.

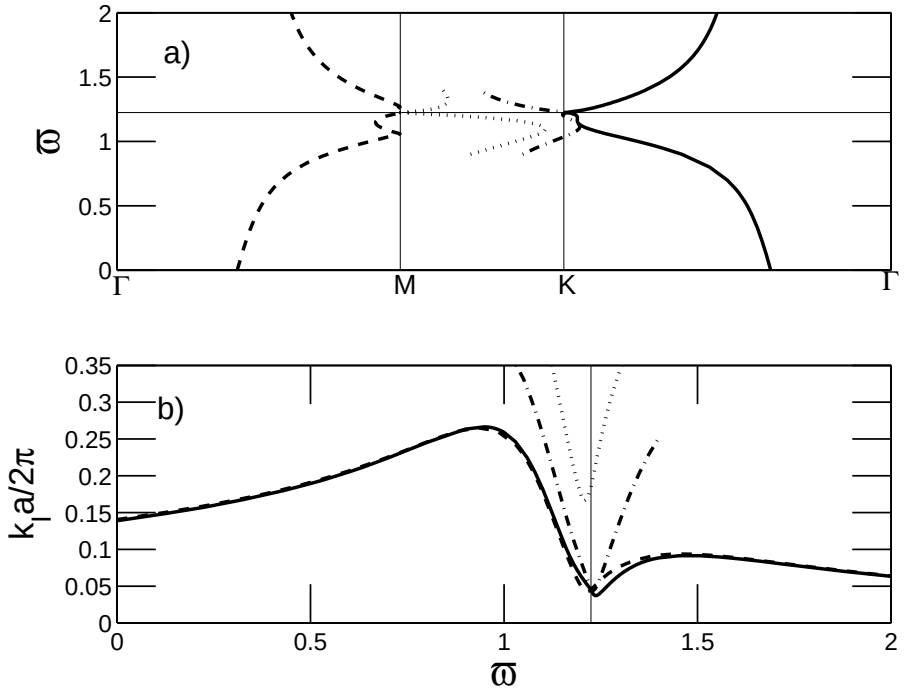

Figure 3.5: (a) TE bands of triangular vortex lattice with frequency dependent dielectric function $\epsilon_{\rm loc}(\varpi)$ (Fig. 3.2b), and (b) imaginary parts of the wave vector k_I corresponding to each mode. Particle density is $N = 6.6 \times 10^{20}$ m^{-3} and lattice constant is $a = 4.5\xi$. Enhancement frequency Ω_0 is tuned to the band gap at the M edge ($\omega_g = 0.31(2\pi c/a)$) of constant dielectric case (Fig. 3.3b). There exists a complete band gap.

Sec. 3.4.2.

In Fig. 3.4b, imaginary parts of the wave vector k_I is plotted for different propagation directions. In the ΓM and ΓK directions only a single band exists within the enhancement window, while for the MK direction there are two bands. At the enhancement frequency $\varpi_0 = 1.22$, two of these bands have zero k_I, while the other two have a complex wave vector. In accordance with the discussion in the previous paragraph, we identify the existence of a pseudo-band gap in the ΓM propagation direction. Thus, incident light (exactly at ϖ_0) would propagate in the ΓK, MK directions while it would be stopped in the ΓM direction.

In the second case, Fig. 3.5, all of the four bands have nonzero k_I at $\varpi = \varpi_0$. This indicates the existence of a complete band gap at the enhancement frequency. Incident light is stopped for all propagation directions.

We see that the conclusions for the existence of photonic band gaps obtained by constant ϵ calculations are not modified, even when the strong frequency dependence of $\epsilon(\omega)$ is taken into account.

The reason of performing such a tuning, as in equation (3.6), is to keep the k_I maximum. The choice of ω_g', in Fig. 3.3, at the center of the gap is not obligatory. As long as ω_g' is chosen in the band gap of constant dielectric, there would be gap at $\varpi = \varpi_0$ in Figs. 3.4 and 3.5. But the stoppage, proportional to k_I, becomes smaller.

Here it is worth to end this section by emphasizing the frequency dimensions of the enhancement window. Dielectric function (3.4) differs from the unity (vacuum) only in the frequency range $\omega = \Omega_0 \pm 5\gamma$ of width $\sim 10^9$Hz. Since the typical lattice parameter in rotating BEC is about $a \sim 200$ nm, the natural lattice frequency $2\pi c/a$ is of order $\sim 10^{15}$ Hz. The latter is six orders of magnitude greater than the former. The index enhancement without absorption, on the other hand, is achievable in a narrower frequency range $\sim 0.1\gamma$. This illustrates the possible width of the band gaps.

3.4.2 Poynting Vector

We demonstrated the existence of both directional and complete band gap at exactly on the enhancement frequency Ω_0. The extent of the band gap about ω_0, however, cannot be argued considering only the k_I values. For a given value of k_I, one cannot distinguish between if the decaying behavior ($e^{-\vec{k}_I \cdot \vec{r}}$) is due to absorption or a band gap.

To be able to define the width of the gap, we also examined the behavior of the complex Poynting vector

$$\vec{S}(\vec{r}) = \frac{1}{2}\vec{E}(\vec{r}) \times \vec{H}(\vec{r})^* \tag{3.7}$$

in the crystal. The real part of the Poynting vector, $\vec{S}_R(\vec{r})$, gives the energy flux of the field at position $\vec{r}$. On the other hand, imaginary part, $\vec{S}_I(\vec{r})$, is a measure of the reactive (stored) energy [100]. When $\epsilon(\omega)$ is real Poynting vector is real on the bands, and purely imaginary on the band gap regions. For a complex $\epsilon(\omega)$, however, the imaginary part of $\vec{S}$ may also be due to the absorption. Despite the similarity of the statements of $\vec{k}_I$ and $\vec{S}_I$, together they are sufficient in the determination of the gap width.

Fourier coefficients, corresponding to each frequency and band, are also calculated in the band computations. Using these coefficients, we calculated spatial average of the Poynting vector, $\langle \vec{S} \rangle$, in the unit cell. We define

$$\alpha = |\langle S_I \rangle| / |\langle S \rangle| \quad , \tag{3.8}$$

as the rate of reactive (stored) energy. Since we aim to investigate the width of the directional gap in Fig. 3.4, $\langle S \rangle$ and $\langle S_I \rangle$ are computed along the ΓM direction.

The width of the gap is decided as follows. In Fig. 3.6, α displays a marked increase near the enhancement frequency. This increase, however, cannot be caused by the imaginary part of $\epsilon_{\text{loc}}(\varpi)$. Because, near the enhancement frequency this imaginary part decreases to zero. Thus, the peak in the reactive energy ratio must be caused by the periodicity of the crystal. The presence of the band gap increases the reactive energy ratio, despite the decreasing absorption.

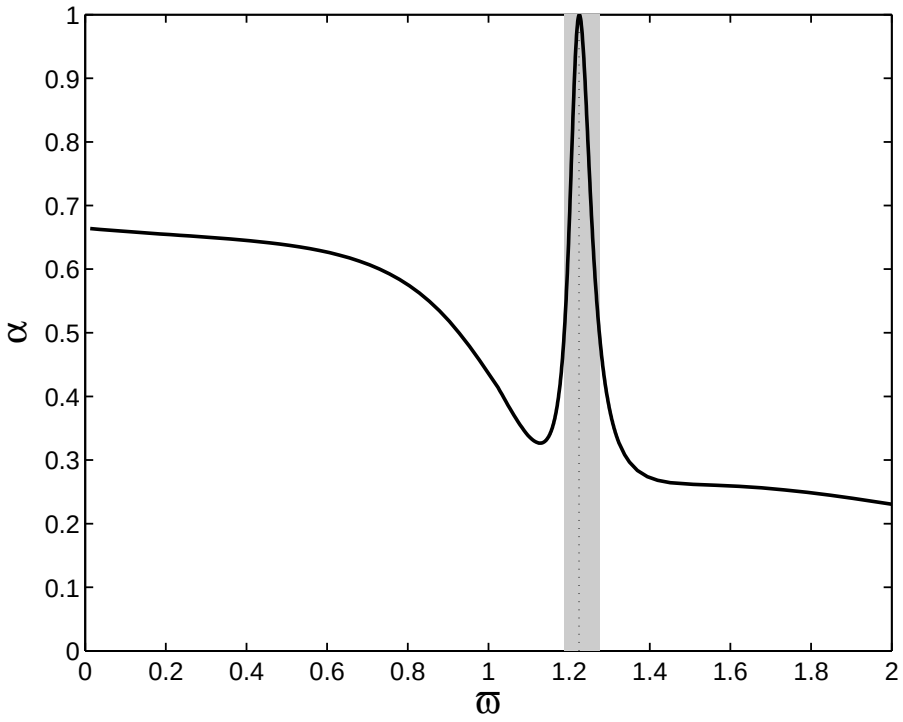

Figure 3.6: Reactive energy ratio α for the ΓM band of Fig. 3.4. Vertical dashed line indicates the enhancement frequency $\varpi_0 = 1.22$. Shaded region is the effective photonic band gap. Width of the peak determines the width of the gap to be $\omega = \Omega \pm 0.043\gamma$ which corresponds to ± 1.65 MHz.

We define the width of the band gap, in Fig. 3.6, as the full width at half maximum (FWHM) at the enhancement frequency. We note that at real dielectric, $\varpi = \varpi_0$, there is no propagation in the crystal ($\alpha = 1$) as expected. Within this definition, we determine an effective band gap in the frequency range $\varpi = \varpi_0 \pm 0.043$. This corresponds to a bandwidth of 3.30 MHz. The same method gives a band gap of width 5.98 MHz for the bands of Fig. 3.5.

Similar calculations for TM modes result in the similar band structure. Directional or complete band gaps are also achievable for TM modes. If the constant dielectric band gaps of TE and TM coincides, they also meat in the band structure of complex frequency-dependent dielectric case.

3.5 Raman Scheme

The index enhancement in the upper-level microwave scheme is strong. However, vanishing absorption is achievable in only $0.04\gamma \simeq 3.3$ MHz frequency interval. In the Raman scheme [87], which is depicted in Fig. 3.7, the frequency interval of zero absorption is broader at least of one order of magnitude, see Fig. 3.8. The dielectric response, in contrast, is one order of magnitude weaker than the microwave scheme [87]. Then, microwave scheme provides a strong band gap (large k_I) at single frequency, but Raman scheme leads a weaker band gap (small k_I) at broader frequency interval.

Dielectric function for the Raman scheme is calculated numerically by solving density matrix equations in the steady state [87] and the results are plotted in the Fig. 3.8. We take the decay rates of the level a onto b and b' equal, since the levels are energetically very close. Because of the same reason, their decay in between is small $\gamma_b = \gamma_{b'} = 10^{-3}\gamma$. The spacing between the b-b' is $\omega_{bb'} = \gamma = \gamma'$. The decay rate of level c on b and b' is $\gamma_c = \gamma_c' = \gamma$. Since the a-c transition is dipole forbidden, $\gamma_a = 10^{-3}\gamma$. The Rabi frequency is $\Omega_R = 5.9\gamma$ and the pump rates are $r = r' = 0.017\gamma$. In Fig. 3.8, we indicated the frequency region of zero absorption with shadow. Between $\varpi = 1.8 - 2.2$ imaginary part χ'' vanishes. The new enhancement is about the frequency $\varpi_0 = 2$. The density used is 500 times

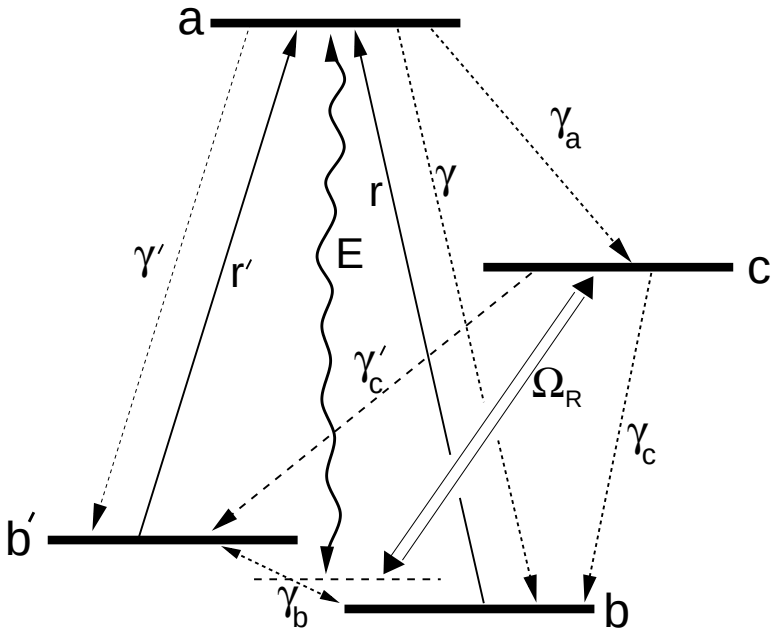

Figure 3.7: Raman scheme for index enhancement. Probe field E, coupling field Ω_R, pumping rates r, r', and decay rates are indicated.

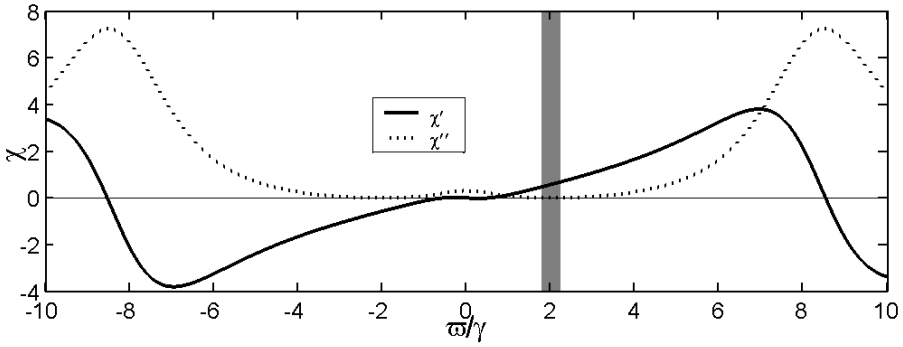

Figure 3.8: Real (solid-line) and imaginary (doted-line) parts of dielectric function, obtained through Raman scheme for particle density $N = 2.3\times10^{23}\mathrm{m}^{-3}$. Shaded area, $\varpi = 1.8 - 2.2$, is the frequency window of zero absorption.

of the one used in the upper-level microwave scheme, Fig. 3.2a.

In Fig. 3.9, frequency independent dielectric constant is used in the band calculation for the Raman scheme. Dielectric constant is chosen at the frequency in the middle of the zero-absorption window, shaded region in the Fig. 3.8.

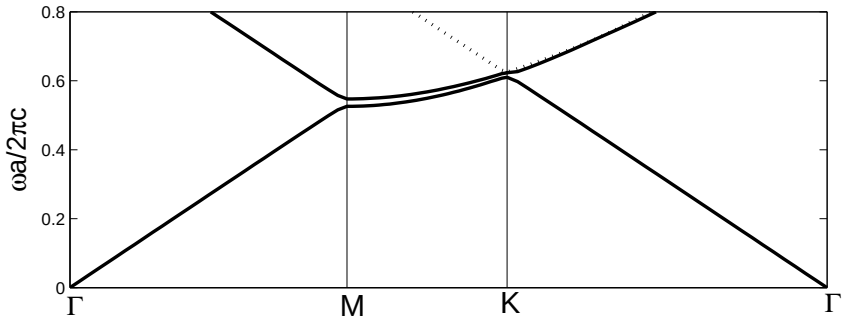

Figure 3.9: Band diagram for TE modes of a triangular vortex lattice with frequency independent $\epsilon = 1.29$ and $a = 10\xi$. Midgap frequency is $0.537(2\pi c/a)$.

In Fig. 3.10 we plotted the photonic bands of a triangular vortex lattice, where index enhancement is achieved via Raman scheme, taking into account frequency dependent complex dielectric function. In the calculation we followed the same methods, described in the Sec. 3.4.1. There is only a directional band gap in the ΓM direction. The frequency width of the gap is clear. There exists band gap in the whole frequency region $\varpi = 1.8 - 2.2$. This corresponds to a frequency width of $0.4\gamma = 31$ MHz. The stoppage of the incident pulse is accomplished after a propagation of about 80 cites.

3.6 Conclusion

We calculated the photonic bands for an index enhanced vortex lattice, considering a frequency dependent complex dielectric function. We review the main conclusions of our previous works [2, 86], that photonic band gaps can be created via index enhancement on vortex lattices of BECs. Specifically, we presented two examples showing that both directional and complete band gaps are possible within experimentally realizable parameter regimes. For the specific parameters and the upper level microwave scheme for index enhancement we considered, band gaps of order a few MHz width are obtained. We also discussed how band gaps are designed for specific parameter values, and how band gap widths can be increased. In particular, using a Raman scheme allows for an

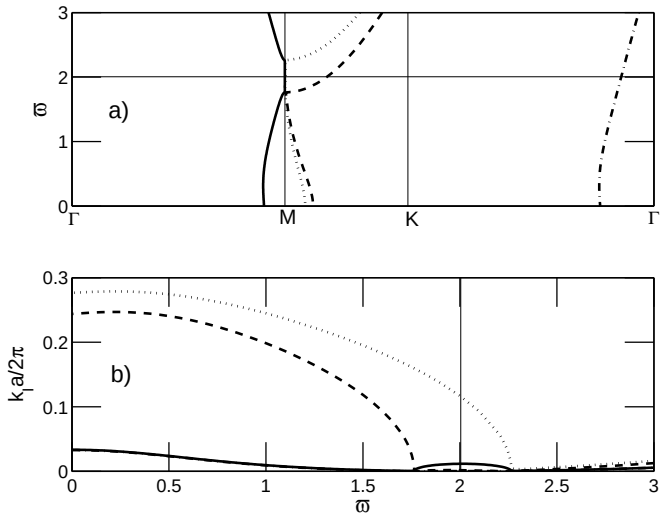

Figure 3.10: TE bands of triangular vortex lattice with Raman index enhancement scheme, dielectric function plotted in Fig. 3.8. There exists a directional gap in the ΓM direction of width $0.4\gamma = 31$MHz.

order of magnitude increase in the band width.

Bibliography

[1] M.E. Taşgın, M.Ö. Oktel, L. You, and Ö.E. Müstecaplıoğlu, Phys. Rev. A **79**, 053603 (2009).

[2] M.E. Taşgın, Ö.E. Müstecaplıoğlu,and M.Ö. Oktel, Phys. Rev. A **75**, 063627 (2007).

[3] M.E. Taşgın, Ö.E. Müstecaplıoğlu,and M.Ö. Oktel, Las. Phys. **19**, 647 (2009).

[4] R. H. Dicke, Phys. Rev. **93**, 99 (1954).

[5] N. Skribanowitz, I. P. Herman, J. C. MacGillivray, and M. S. Feld, Phys. Rev. Lett. **30**, 309 (1973).

[6] M. Sargent, M.O. Scully, W.E. Lamb, *Laser Physics* (Mass.: Addison-Wesley, 1974).

[7] L. Mandel and E. Wolf, *Optical Coherence and Quantum Optics* (Cambridge University Press, Cambridge, 1995).

[8] S. Slama, S. Bux, G. Krenz, C. Zimmermann, and Ph.W. Courteille, Phys. Rev. Lett.**98**, 053603 (2007).

[9] M.M. Cola, D. Bigerni, and N. Piovella, Phys. Rev. A **79**, 053622 (2009).

[10] R. Bonifacio and L. A. Lugiato, Phys. Rev. A **11**, 1507 (1975); *ibid.* **12**, 587 (1975).

[11] F. T. Arecchi and E. Courtens, Phys. Rev. A **2**, 1730 (1970).

[12] N. E. Rehler and J. H. Eberly, Phys. Rev. A **3**, 1735 (1971).

[13] M. Gross and S. Haroche, Phys. Rep. **93**, 301 (1982).

[14] Q. H. F. Vrehen, H. M. J. Hikspoors, and H. M. Gibbs, Phys. Rev. Lett. **38**, 764 (1977).

[15] Y. N. Chen, D. S. Chuu, and T. Brandes, Phys. Rev. Lett. **90**, 166802 (2003).

[16] Y. N. Chen, C. M. Li, D. S. Chuu, and T. Brandes, New Jour. Phys. **7**, 172 (2005).

[17] A. Mitra, R. Vyas, and D. Erenso, Phys. Rev. A **76**, 052317 (2007).

[18] T. Wang, S. F. Yelin, R. Côté, E. E. Eyler, S. M. Farooqi, P. L. Gould, M. Koštrun, D. Tong, and D. Vrinceanu, Phys. Rev. A **75**, 033802 (2007).

[19] V. I. Yukalov, Laser Phys. **12**, 1089 (2002); V. I. Yukalov, and E. P. Yukalova, Laser Phys. Lett. **2**, 302 (2005); V. I. Yukalov, Phys. Rev. B **71**, 184432 (2005); V. I. Yukalov, Laser Phys. Lett. **2**, 356 (2005); V. I. Yukalov, V. K. Henner, and P. V. Kharebov, Phys. Rev. B **77**, 134427 (2008); V. I. Yukalov, V. K. Henner, P. V. Kharebov, and E. P. Yukalova, Laser Phys. Lett. **5**,887 (2008).

[20] S. Inouye, A.P. Chikkatur, D.M. Stamper-Kurn, J. Stenger, D.E. Pritchard, and W. Ketterle, Science **285**, 571 (1999).

[21] J.S. Bell, Physics **1**, 195 (1965).

[22] J.S. Bell, *Foundation of Quantum Mechanics*, edited by B. d'Espagnat (Academic, New York, 1971), p. 171.

[23] A. Einstein, B. Podolsky, and N. Rosen, Phys. Rev. **47**, 777 (1935).

[24] J.J. Sakurai, *Modern Quantum Mechanics*, (Menlo Park, Calif.: Benjamin/Cummings, 1985).

[25] Z.Y. Ou, S.F. Pereira, H.J. Kimble, and K.C. Peng, Phys. Rev. Lett.**68**, 3663 (1992).

[26] W.P. Bowen, R. Schnabel, P.K. Lam, and T.C. Ralph, Phys. Rev. Lett.**90**, 043601 (2003).

[27] C. Schori, J.L. Sorensen, and E.S. Polzik, Phys. Rev. A **66**, 033802 (2002).

[28] A.S. Villar, L.S. Cruz, K.N. Cassemiro, M. Martinelli, and P. Nussenzveig, Phys. Rev. Lett.**95**, 243603 (2005).

[29] [5] V. Josse, A. Dantan, A. Bramati, M. Pinard, and E. Giacobino, Phys. Rev. Lett.**92**, 123601 (2004).

[30] Y.-J. Xia and G.-C. Guo, Chin. Phys. Lett. **21**, 1877 (2004).

[31] Y. Ping, B. Zhang, Z. Cheng, and Y. Zhang, Phys. Lett. A **362**, 128 (2007).

[32] N.A. Ansari, Phys. Rev. A **55**, 1639 (1997).

[33] H.-T. Tan, S.-Y. Zhu, and M.S. Zubairy, Phys. Rev. A **72**, 022305 (2005).

[34] H. Xiong, M.O. Scully, and M.S. Zubairy, Phys. Rev. Lett.**94**, 023601 (2005).

[35] A. Furusawa, J.L. Sorensen, S.L. Braunstein, C.A. Fuchs, H.J. Kimble, and E.S. Polzik, Science **282** 706 (1998).

[36] L. Vaidman, Phys. Rev. A **49**, 1473 (1994).

[37] S.L. Braunstein, Phys. Rev. Lett.**80** 869 (1998).

[38] A.K. Ekert, Phys. Rev. Lett.**67**, 661 (1991).

[39] A. Barenco, D. Deutsch, and A. Ekert, Phys. Rev. Lett.**74**, 4083 (1995).

[40] S.L. Braunstein, Nature **394**, 47 (1998).

[41] S. Lloyd, Phys. Rev. Lett.**82**, 1784 (1999).

[42] A.S. Parkins, and H.J. Kimble, J. Opt. B: Quantum Semiclass. Opt. **1**, 496 (1999).

[43] M.G. Moore and P. Meystre, Phys. Rev. Lett. **85**, 5026 (2000).

[44] M.G. Moore, O. Zobay, and P. Meystre, Phys. Rev. A **60**, 1491 (1999).

[45] M.G. Moore and P. Meystre, Phys. Rev. A **59**, R1754 (1999).

[46] D. Schneble *et al.*, Science **300**, 475 (2003).

[47] H. Pu, W. Zhang, and P. Meystre, Phys. Rev. Lett. **91**, 150407 (2003).

[48] M. Żukowski, A. Zeilinger, M. A. Horne, and A. K. Ekert, Phys. Rev. Lett. **71**, 4287 (1993).

[49] C. H. Bennett, G. Brassard, C. Crépeau, R. Jozsa, A. Peres, and W. K. Wootters, Phys. Rev. Lett. **70**, 1895 (1993).

[50] S. Bose, V. Vedral, and P. L. Knight, Phys. Rev. A **57**, 822 (1998).

[51] J.-W. Pan, D. Bouwmeester, H. Weinfurter, and A. Zeilinger, Phys. Rev. Lett. **80**, 3891 (1998).

[52] O. Zobay and G. M. Nikolopoulos, Phys. Rev. A **73**, 013620 (2006).

[53] G. M. R. Robb, N. Piovella, and R. Bonifacio, J. Opt. B: Quantum Semiclassical Opt. **7**, 93 (2005).

[54] C. Benedek and M. G. Benedikt, J. Opt. B: Quantum Semiclassical Opt. **6**, S111 (2004).

[55] N. A. Vasil'ev, O. B. Efimov, E. D. Trifonov, and N. I. Shamrov, Laser Phys. **14**, 1268 (2004).

[56] H. Pu and P. Meystre, Phys. Rev. Lett. **85**, 3987 (2000).

[57] J. C. Howell, R. S. Bennink, S. J. Bentley, and R. W. Boyd, Phys. Rev. Lett. **92**, 210403 (2004).

[58] M. D'Angelo, Y.-H. Kim, S. P. Kulik, and Y. Shih, Phys. Rev. Lett. **92**, 233601 (2004).

[59] A. V. Andreev, V. I. Emel'yanov, and Y. A. Il'inskiĭ, *Cooperative Effects in Optics: Superradiance and Phase Transitions* (Bristol: Institute of Physics, 1993).

[60] D. Polder, M. F. H. Schuurmans, and Q. H. F. Vrehen, Phys. Rev. A **19**, 1192 (1979).

[61] L. You, J. Cooper, and M. Trippenbach, Jour. Opt. Soc. Am. B **8**, 1139 (1991).

[62] M. G. Moore and P. Meystre, Phys. Rev. Lett. **83**, 5202 (1999).

[63] M. Lewenstein, L. You, J. Cooper, and K. Burnett, Phys. Rev. A **50**, 2207 (1994).

[64] L. You, M. Lewenstein, and J. Cooper, Phys. Rev. A **51**, 4712 (1995).

[65] L. You, M. Lewenstein, R.J. Glauber, and J. Cooper, Phys. Rev. A **53**, 329 (1996).

[66] O. E. Mustecaplioglu and L. You, Phys. Rev. A **62**, 063615 (2000).

[67] L.M. Duan, G. Giedke, J.I. Cirac, and P. Zoller, Phys. Rev. Lett. **84**, 2722 (2000).

[68] A. Peres, Phys. Rev. Lett. **77**, 1413 (1996).

[69] R.F. Werner, Phys. Rev. A **40**, 4277 (1989).

[70] M.D. Reid and D.F. Walls, Phys. Rev. A **34**, 1260 (1986).

[71] M. G. A. Paris, M. Cola, N. Piovella, and R. Bonifacio, Optics Commun. **227**, 349 (2003).

[72] D.C. Burnham, and R.Y. Chiao. Phys. Rev. **188**, 667 (1969)

[73] M.O. Scully and M.S. Zubairy, *Quantum Optics* (Cambridge University Press, Cambridge, 1997).

[74] H. Uys and P. Meystre, Phys. Rev. Lett.**75**, 033805 (2007).

[75] J. R. Abo-Shaeer, C. Raman, J. M. Vogels, and W. Ketterle, Science **292**, 476 (2001).

[76] P.C. Haljan, I. Coddington, P. Engels, and E.A. Cornell, Phys. Rev. Lett. **87**, 210403 (2001).

[77] T.-L. Ho, Phys. Rev. Lett. **87**, 060403 (2001).

[78] G. Baym and C.J. Pethick, Phys. Rev. A **69**, 043619 (2004).

[79] P. Engels, I. Coddington, P.C. Haljan, and E.A. Cornell, Phys. Rev. Lett. **89**, 100403 (2002).

[80] V. Schweikhard, I. Coddington, P. Engels, S. Tung, and E.A. Cornell, Phys. Rev. Lett. **93**, 210403 (2004).

[81] K.W. Madison, F. Chevy, W. Wohlleben, and J. Dalibard, Phys. Rev. Lett. **84**, 806 (2000).

[82] K.W. Madison, F. Chevy, V. Bretin, and J. Dalibard, Phys. Rev. Lett. **86**, 4443 (2001).

[83] N.L. Smith, W.H. Heathcote, J.M. Krueger, and C.J. Foot, Phys. Rev. Lett. **93**, 080406 (2004).

[84] J.D. Joannopoulos, R.D. Meade and J.N. Winn, *Photonic crystals : molding the flow of light* (Princeton University Press, Princeton, 1995).

[85] S.L. Cornish, N.R. Claussen, J.L. Roberts, E.A. Cornell and C.E. Wieman, Phys. Rev. Lett. **85**, 1795 (2000).

[86] Ö.E. Müstecaplıoğlu and M.Ö. Oktel, Phys. Rev. Lett. **94**, 220404 (2005).

[87] M. Fleischhauer, C.H. Keitel, M.O. Scully, C. Su, B.T. Ulrich, and S.Y. Zhu, Phys. Rev. A **46**, 1468 (1992).

[88] A.A. Krokhin and P. Halevi, Phys. Rev. B **53**, 1205 (1996).

[89] M.M. Sigalas, C.M. Soukoulis, C.T. Chan, and K.M. Ho, Phys. Rev. B **49**, 11080 (1994).

[90] V. Kuzmiak and A.A. Maradudin, Phys. Rev. **55**, 7427 (1997).

[91] L.-M. Li, Z.-Q. Zhang and X. Zhang, Phys. Rev. B **58**, 15589 (1998).

[92] A. Moroz, A. Tip, and J.-M. Combes, Synthetic Mat. in press. (2000).

[93] A. Tip, A. Moroz, and J.M. Combes, J.Phys.A:Math.Gen. **33**, 6223 (2000).

[94] H. van der Lem, A. Tip, A. Moroz, J. Opt. Soc. Am. B**20**, 1334 (2003).

[95] X. Jiang and C.M. Soukoulis, Phys. Rev. B **59**, 6159 (1999).

[96] G. Veronis, R. W. Dutton, and S. Fan, J. App. Phys. **97**, 093104 (2005).

[97] J. Ruostekoski and J. Javanainen, Phys. Rev. Lett.**82**, 4741 (1999);M. Fleischhauer, Phys. Rev. A **60**, 2534 (1999); H. Wallis, ibid. **56**, 2060 (1997); O. Morice, Y. Castin, and J. Dalibard, ibid. **51**, 3896 (1995); J. Ruostekoski and J. Javanainen, ibid. **56**, 2056 (1997); K. V. Krutitsky, K.-P. Marzlin, and J. Audretsch, ibid. **65**, 063609 (2002).

[98] N. G. Berloff, J. Phys. A **37**, 1617 (2004).

[99] A. Tip, A. Moroz, and J. M. Combes, J. Phys. A **33**, 6223 (2000). C. Kittel, *Introduction to Solid State Physics* (John Wiley & Sons Inc., New York, 1996).

[100] J.D. Jackson, *Classical Electrodynamics* (John Wiley & Sons Inc., New York, 1999).